CLNS 97/1477
CLEO 97-7
CLEO CONF 97-10
EPS abstract 703
Submitted to PRD

Measurements of the Meson-Photon Transition Form Factors of Light Pseudoscalar Mesons at Large Momentum Transfer

CLEO Collaboration
(July 10, 1997)

Using the CLEO II detector, we have measured the differential cross sections for exclusive two-photon production of light pseudoscalar mesons π^0, η, and η'. From our measurements we have obtained the form factors associated with the electromagnetic transitions $\gamma^*\gamma \to$ meson. We have measured these form factors in the momentum transfer ranges from 1.5 to 9, 20, and 30 GeV^2 for π^0, η, and η', respectively, and have made comparisons to various theoretical predictions.

12.38.Qk,13.40.Gp,13.65.+i

J. Gronberg,[1] T. S. Hill,[1] R. Kutschke,[1] D. J. Lange,[1] S. Menary,[1] R. J. Morrison,[1] H. N. Nelson,[1] T. K. Nelson,[1] C. Qiao,[1] J. D. Richman,[1] D. Roberts,[1] A. Ryd,[1] M. S. Witherell,[1] R. Balest,[2] B. H. Behrens,[2] W. T. Ford,[2] H. Park,[2] J. Roy,[2] J. G. Smith,[2] J. P. Alexander,[3] C. Bebek,[3] B. E. Berger,[3] K. Berkelman,[3] K. Bloom,[3] D. G. Cassel,[3] H. A. Cho,[3] D. M. Coffman,[3] D. S. Crowcroft,[3] M. Dickson,[3] P. S. Drell,[3] K. M. Ecklund,[3] R. Ehrlich,[3] R. Elia,[3] A. D. Foland,[3] P. Gaidarev,[3] R. S. Galik,[3] B. Gittelman,[3] S. W. Gray,[3] D. L. Hartill,[3] B. K. Heltsley,[3] P. I. Hopman,[3] J. Kandaswamy,[3] P. C. Kim,[3] D. L. Kreinick,[3] T. Lee,[3] Y. Liu,[3] G. S. Ludwig,[3] J. Masui,[3] J. Mevissen,[3] N. B. Mistry,[3] C. R. Ng,[3] E. Nordberg,[3] M. Ogg,[3,1] J. R. Patterson,[3] D. Peterson,[3] D. Riley,[3] A. Soffer,[3] B. Valant-Spaight,[3] C. Ward,[3] M. Athanas,[4] P. Avery,[4] C. D. Jones,[4] M. Lohner,[4] C. Prescott,[4] J. Yelton,[4] J. Zheng,[4] G. Brandenburg,[5] R. A. Briere,[5] Y. S. Gao,[5] D. Y.-J. Kim,[5] R. Wilson,[5] H. Yamamoto,[5] T. E. Browder,[6] F. Li,[6] Y. Li,[6] J. L. Rodriguez,[6] T. Bergfeld,[7] B. I. Eisenstein,[7] J. Ernst,[7] G. E. Gladding,[7] G. D. Gollin,[7] R. M. Hans,[7] E. Johnson,[7] I. Karliner,[7] M. A. Marsh,[7] M. Palmer,[7] M. Selen,[7] J. J. Thaler,[7] K. W. Edwards,[8] A. Bellerive,[9] R. Janicek,[9] D. B. MacFarlane,[9] K. W. McLean,[9] P. M. Patel,[9] A. J. Sadoff,[10] R. Ammar,[11] P. Baringer,[11] A. Bean,[11] D. Besson,[11] D. Coppage,[11] C. Darling,[11] R. Davis,[11] N. Hancock,[11] S. Kotov,[11] I. Kravchenko,[11] N. Kwak,[11] S. Anderson,[12] Y. Kubota,[12] M. Lattery,[12] S. J. Lee,[12] J. J. O'Neill,[12] S. Patton,[12] R. Poling,[12] T. Riehle,[12] V. Savinov,[12] A. Smith,[12] M. S. Alam,[13] S. B. Athar,[13] Z. Ling,[13] A. H. Mahmood,[13] H. Severini,[13] S. Timm,[13] F. Wappler,[13] A. Anastassov,[14] S. Blinov,[14,2] J. E. Duboscq,[14] K. D. Fisher,[14] D. Fujino,[14,3] K. K. Gan,[14] T. Hart,[14] K. Honscheid,[14] H. Kagan,[14] R. Kass,[14] J. Lee,[14] M. B. Spencer,[14] M. Sung,[14] A. Undrus,[14,2] R. Wanke,[14] A. Wolf,[14] M. M. Zoeller,[14] B. Nemati,[15] S. J. Richichi,[15] W. R. Ross,[15] P. Skubic,[15] M. Bishai,[16] J. Fast,[16] E. Gerndt,[16] J. W. Hinson,[16] N. Menon,[16] D. H. Miller,[16] E. I. Shibata,[16] I. P. J. Shipsey,[16] M. Yurko,[16] L. Gibbons,[17] S. Glenn,[17] S. D. Johnson,[17] Y. Kwon,[17] S. Roberts,[17] E. H. Thorndike,[17] C. P. Jessop,[18] K. Lingel,[18] H. Marsiske,[18] M. L. Perl,[18] D. Ugolini,[18] R. Wang,[18] X. Zhou,[18] T. E. Coan,[19] V. Fadeyev,[19] I. Korolkov,[19] Y. Maravin,[19] I. Narsky,[19] V. Shelkov,[19] J. Staeck,[19] R. Stroynowski,[19] I. Volobouev,[19] J. Ye,[19] M. Artuso,[20] A. Efimov,[20] F. Frasconi,[20] M. Gao,[20] M. Goldberg,[20] D. He,[20] S. Kopp,[20] G. C. Moneti,[20] R. Mountain,[20] S. Schuh,[20] T. Skwarnicki,[20] S. Stone,[20] G. Viehhauser,[20] X. Xing,[20] J. Bartelt,[21] S. E. Csorna,[21] V. Jain,[21] S. Marka,[21] R. Godang,[22] K. Kinoshita,[22] I. C. Lai,[22] P. Pomianowski,[22] S. Schrenk,[22] G. Bonvicini,[23] D. Cinabro,[23] R. Greene,[23] L. P. Perera,[23] G. J. Zhou,[23] B. Barish,[24] M. Chadha,[24] S. Chan,[24] G. Eigen,[24] J. S. Miller,[24] C. O'Grady,[24] M. Schmidtler,[24] J. Urheim,[24] A. J. Weinstein,[24] F. Würthwein,[24] D. M. Asner,[25] D. W. Bliss,[25] G. Masek,[25] H. P. Paar,[25] S. Prell,[25] M. Sivertz,[25] and V. Sharma[25]

[1]University of California, Santa Barbara, California 93106
[2]University of Colorado, Boulder, Colorado 80309-0390
[3]Cornell University, Ithaca, New York 14853
[4]University of Florida, Gainesville, Florida 32611
[5]Harvard University, Cambridge, Massachusetts 02138
[6]University of Hawaii at Manoa, Honolulu, Hawaii 96822
[7]University of Illinois, Champaign-Urbana, Illinois 61801
[8]Carleton University, Ottawa, Ontario, Canada K1S 5B6
and the Institute of Particle Physics, Canada
[9]McGill University, Montréal, Québec, Canada H3A 2T8
and the Institute of Particle Physics, Canada
[10]Ithaca College, Ithaca, New York 14850
[11]University of Kansas, Lawrence, Kansas 66045
[12]University of Minnesota, Minneapolis, Minnesota 55455
[13]State University of New York at Albany, Albany, New York 12222
[14]Ohio State University, Columbus, Ohio 43210
[15]University of Oklahoma, Norman, Oklahoma 73019
[16]Purdue University, West Lafayette, Indiana 47907
[17]University of Rochester, Rochester, New York 14627

[1]Permanent address: University of Texas, Austin TX 78712
[2]Permanent address: BINP, RU-630090 Novosibirsk, Russia.
[3]Permanent address: Lawrence Livermore National Laboratory, Livermore, CA 94551.

[18]Stanford Linear Accelerator Center, Stanford University, Stanford, California 94309
[19]Southern Methodist University, Dallas, Texas 75275
[20]Syracuse University, Syracuse, New York 13244
[21]Vanderbilt University, Nashville, Tennessee 37235
[22]Virginia Polytechnic Institute and State University, Blacksburg, Virginia 24061
[23]Wayne State University, Detroit, Michigan 48202
[24]California Institute of Technology, Pasadena, California 91125
[25]University of California, San Diego, La Jolla, California 92093

I. INTRODUCTION

Production of even C-parity hadronic matter in e^+e^- scattering provides a unique opportunity to study the properties of strong interactions. To leading order in quantum electrodynamics (QED) these processes are described as the interaction between two photons emitted by the scattered electrons[4]. Although in e^+e^- scattering the probe and the target are both represented by photons that are carriers of the electromagnetic force, these space-like photons can produce a pair of quarks that interact strongly and are observed in the form of hadrons. Therefore, by measuring the four-momenta of the scattered electrons we can study the dynamics of strong interactions. The quantities of interest in these studies are the form factors associated with the transitions between the photons and the hadrons.

This Article describes the measurements [1] of the differential cross sections for the production of a single pseudoscalar meson in e^+e^- scattering:

$$e^+e^- \to e^+e^-\mathcal{R}, \tag{1}$$

where $\mathcal{R}$ is a π^0, η or η'. We measure these cross sections in a "single-tagged" experimental mode where one of the scattered electrons is detected ("tagged"), while the other electron is scattered at a very small angle and therefore remains undetected ("*un*tagged"). The mesons produced in e^+e^- scattering are observed through their decays to various fully reconstructed final states. The tagged electron emits a highly off-shell photon (γ^*), whereas the untagged electron emits a nearly on-shell photon (γ). We measure the dependence of the meson production rate on the squared momentum transfer Q^2 carried by the highly off-shell photon. This momentum transfer is determined by energy-momentum conservation as applied to the tag:

$$Q^2 \equiv -(p_b - p_t)^2 = 2E_bE_t(1-\cos\theta_t), \tag{2}$$

where p_b and p_t are the four-momenta of the incident beam-energy electron and the tag, E_b and E_t are corresponding energies, and θ_t is the scattering angle[5]. From the measurements of the differential rates

$$\frac{d\sigma(e^+e^- \to e^+e^-\mathcal{R})}{dQ^2} \tag{3}$$

we obtain the transition form factors $\mathcal{F}_{\gamma^*\gamma\mathcal{R}}$ that describe the effect of the strong interaction in the $\gamma^*\gamma \to \mathcal{R}$ transition amplitudes.

To relate the differential cross sections to the transition form factors we employ the theoretical framework developed by V.M. Budnev *et al.* [2] (BGMS formalism). In BGMS the process $e^+e^- \to e^+e^-\mathcal{R}$ is divided into two parts: $e^+e^- \to e^+e^-\gamma^*\gamma$ and $\gamma^*\gamma \to \mathcal{R}$. The first part is completely calculable in QED and the second part is defined in terms of the transition form factors $\mathcal{F}_{\gamma^*\gamma\mathcal{R}}(Q^2)$. In the case of pseudoscalar mesons there is only one form factor. At zero momentum transfer this form factor is expressed as:

$$|\mathcal{F}_{\gamma^*\gamma\mathcal{R}}(0)|^2 = \frac{1}{(4\pi\alpha)^2}\,\frac{64\pi\Gamma(\mathcal{R}\to\gamma\gamma)}{M_{\mathcal{R}}^3}\,, \tag{4}$$

where α is the QED coupling constant, $M_{\mathcal{R}}$ is the mass and $\Gamma(\mathcal{R}\to\gamma\gamma)$ is the two-photon partial width of the meson $\mathcal{R}$. The transition form factors cannot be calculated directly from Quantum Chromodynamics (QCD). However, they have been estimated using perturbative QCD (PQCD), a sum-rules approach, and other theoretical methods.

One of the important concepts of PQCD-based methods is a factorization procedure that separates perturbative short-distance effects from non-perturbative long-distance ones. While the former are understood well and can be calculated using PQCD, the latter are known only asymptotically, in the limit $Q^2 \to \infty$. In PQCD-based calculations the transition form factor $\mathcal{F}_{\gamma^*\gamma\mathcal{R}}$ is expressed as a convolution of a perturbative Hard Scattering Amplitude (HSA) [3] and the soft non-perturbative wave function of the meson.

Brodsky and Lepage employed PQCD to find the asymptotic behavior of the $\gamma^*\gamma \to \mathcal{R}$ transition form factors in the limit $Q^2 \to \infty$ [4]:

$$\lim_{Q^2\to\infty} Q^2\mathcal{F}_{\gamma^*\gamma\mathcal{R}}(Q^2) = 2f_{\mathcal{R}}, \tag{5}$$

where $f_{\mathcal{R}}$ is the meson decay constant. In addition, it has been predicted that in this limit any mesonic wave function evolves to the asymptotic wave function of unique shape [3,5,6].

[4] Unless otherwise specified, we use the term "electron" for either an electron or a positron.

[5] The electron mass is neglected in Eqn. 2.

While PQCD predicts the form factors of the $\gamma^*\gamma \to \mathcal{R}$ transitions at large momentum transfer, the behavior of these form factors in the limit $Q^2 \to 0$ can be determined from the axial anomaly [7,8] in the chiral limit of QCD. For π^0 and η the axial anomaly yields [4]:

$$\lim_{Q^2\to 0} \mathcal{F}_{\gamma^*\gamma\mathcal{R}}(Q^2) = \frac{1}{4\pi^2 f_{\mathcal{R}}}, \tag{6}$$

to leading order in $m_u^2/M_{\mathcal{R}}^2$ and $m_d^2/M_{\mathcal{R}}^2$ where m_u and m_d are the masses of the u and d quarks. This prediction does not hold with the same precision for η' due to the larger value of the s-quark mass. In addition, even if the s-quark mass were small, this prediction might be broken for η' because this particle is an unlikely candidate for the Goldstone boson [9,10].

To describe the soft non-perturbative region of Q^2 a simple interpolation between $Q^2 \to 0$ and $Q^2 \to \infty$ limits has been proposed [4]:

$$\mathcal{F}_{\gamma^*\gamma\mathcal{R}}(Q^2) \sim \frac{1}{4\pi^2 f_{\mathcal{R}}} \frac{1}{1+(Q^2/8\pi^2 f_{\mathcal{R}}^2)}. \tag{7}$$

To quantify the long-distance effects in the soft non-perturbative region, Chernyak and Zhitnitsky employed the sum-rules method [11] to derive the wave function of the pion at experimentally accessible momentum transfers (the CZ wave function) [6]. They demonstrated that the proposed wave function successfully describes experimental data on the χ_c decay into two pions and the electromagnetic form factor of the charged pion. However, because the theoretical predictions for these processes depend on the strong interaction coupling constant α_s, this introduced a large uncertainty in the determination of the CZ wave function.

Since the asymptotic and CZ wave functions were proposed, they have often been used to describe the non-perturbative parts of transition amplitudes in various PQCD calculations. Jakob, Kroll, and Raulfs employed these wave functions and PQCD to calculate $\mathcal{F}_{\gamma^*\gamma\pi^0}$ [12,13]. These authors have also taken into account small QCD radiative corrections, incorporated into the PQCD technique by Lee and Sterman [14]. Kroll has concluded that the CZ wave function disagrees with our preliminary results [15]. On the contrary, a competing perturbative analysis of Cao, Huang, and Ma [16] yielded that either the asymptotic or the CZ wave function is sufficient to describe the data. These authors took into account quark transverse momentum corrections and neglected the QCD radiative corrections, estimating the latter as small.

While PQCD-based methods are often employed to predict rates for exclusive processes[6], the applicability of these methods at experimentally accessible momentum transfers remains one of the outstanding problems of the theory of strong interactions. Extensive discussion of the validity of the PQCD approach can be found in the literature [22–28].

To avoid ambiguities of the PQCD-inspired calculations at Q^2 of the order of several GeV^2, Radyushkin *et al.* developed an approach [29–31] based on the sum-rules method [11] that they employed to predict the $\gamma^*\gamma \to \pi^0$ transition form factor [32]. This prediction depends on the model of the hadronic spectrum chosen to describe an almost real photon emitted by the untagged electron. It also depends on the values of vacuum condensates which represent non-perturbative matrix elements. The theoretical result of Radyushkin *et al.* reproduces the PQCD-predicted $1/Q^2$ shape of the transition form factor but disagrees with the absolute value given by Eqn. 5 by about 15% in the limit $Q^2 \to \infty$. The authors have stressed that this discrepancy is irrelevant in the region of Q^2 below 10 GeV^2 and could, in principle, be eliminated by including the QCD evolution into the theoretical analysis [33]. It should be noted that the discussed theoretical analysis exactly reproduces the asymptotic prediction of PQCD given by Eqn. 5 when both photons are highly off-mass shell. We should emphasize that at present the non-perturbative treatment of various exclusive processes in a way similar to the approach of Radyushkin *et al.* is the subject of significant theoretical interest. For example, the QCD sum-rules method has been employed recently to predict the form factors in the semileptonic decays of the B mesons[7] [34–36].

The $\gamma^*\gamma \to \mathcal{R}$ transition form factors have been studied by several experiments. The LEPTON-G experiment measured $\mathcal{F}_{\gamma^*\gamma\eta}$ and $\mathcal{F}_{\gamma^*\gamma\eta'}$ in the time-like momentum transfer region up to 0.24 GeV^2 using the rare electromagnetic decays $\eta \to \mu^+\mu^-\gamma$ and $\eta' \to \mu^+\mu^-\gamma$ [47]. In order to achieve higher values of Q^2, the space-like photons produced in two-photon interactions were utilized by the PLUTO experiment to measure $\mathcal{F}_{\gamma^*\gamma\eta'}$ up to 1 GeV^2 [48] and by the TPC/2γ collaboration to study $\mathcal{F}_{\gamma^*\gamma\eta}$ and $\mathcal{F}_{\gamma^*\gamma\eta'}$ up to 7 GeV^2 [49]. More recently, the CELLO experiment measured $\mathcal{F}_{\gamma^*\gamma\pi^0}$ at Q^2 up to 2.7 GeV^2 and $\mathcal{F}_{\gamma^*\gamma\eta}$ and $\mathcal{F}_{\gamma^*\gamma\eta'}$ at Q^2 up to 3.4 GeV^2 [50].

---

[6] For example, these methods have been utilized to calculate the nucleon form factors [17,18] and the $\bar{B}^0 \to \pi^+\pi^-$ branching fraction [19]; see also [20,21].

[7] Recent results of other theoretical developments relevant to our experimental study can be found in the literature [37–46].

We employ two-photon interactions to measure the transition form factors $\mathcal{F}_{\gamma^*\gamma\mathcal{R}}$ in the space-like regions of the momentum transfer between 1.5 and 9 GeV^2 for π^0, 1.5 and 20 GeV^2 for η, and 1.5 and 30 GeV^2 for η'. We study the transition form factors of π^0, η, and η' using the decays:

$$\pi^0 \to \gamma\gamma,$$

$$\eta \to \gamma\gamma,$$

$$\eta \to \pi^0\pi^0\pi^0 \to 6\gamma,$$

$$\eta \to \pi^+\pi^-\pi^0 \to \pi^+\pi^- 2\gamma,$$

$$\eta' \to \rho^0\gamma \to \pi^+\pi^-\gamma,$$

$$\eta' \to \pi^+\pi^-\eta \to \pi^+\pi^- 2\gamma,$$

$$\eta' \to \pi^0\pi^0\eta \to 6\gamma,$$

$$\eta' \to \pi^+\pi^-\eta \to 2\pi^+ 2\pi^- 2\gamma,$$

$$\eta' \to \pi^0\pi^0\eta \to 5\pi^0 \to 10\gamma,$$

$$\eta' \to \pi^0\pi^0\eta \to 3\pi^0\pi^+\pi^- \to \pi^+\pi^- 6\gamma,$$

$$\eta' \to \pi^+\pi^-\eta \to \pi^+\pi^- 3\pi^0 \to \pi^+\pi^- 6\gamma.$$

We analyze the last two decay chains of η' together since they are observed in the same final state $\pi^+\pi^-6\gamma$.

This paper is structured as follows: Section II describes the CLEO II detector and the data sample that we use for our measurements. Event selection criteria, experimental technique, and the analysis procedure for $\gamma\gamma$ final states are explained in Section III. Analyses of other final states with only photons are described in Section IV and analyses of final states with charged pions are described in Section V. The unfolding procedure for the transition form factors is described in Section VI. The results are compared with some existing theoretical predictions in Section VII. Conclusions are presented in Section VIII.

II. EXPERIMENTAL APPARATUS AND MONTE CARLO SIMULATION

A. The CLEO II Detector and Data Sample

The CLEO II detector [51] is a general-purpose magnetic spectrometer which provides energy and momentum measurements for elementary particles. It is operated at the Cornell Electron Storage Ring (CESR), a symmetric e^+e^- collider running at a center-of-mass energy near 10.6 GeV. The major objectives of the CLEO experiment are the studies of the properties of heavy mesons that contain b or c quarks. However, owing to the versatility of the detector, analyses of tagged and untagged two-photon interactions, detailed studies of τ-lepton decays, and careful examination of quark and gluon fragmentation and other processes are also possible.

The active components of CLEO II include central tracking detectors, time-of-flight (TF) scintillator counters, muon detectors, and a CsI calorimeter for electromagnetic showers. The calorimeter consists of a barrel part covering polar angles above 37° and two endcap parts each covering the region between 13° and 37°, where the polar angle is measured with respect to the beam axis. The energy resolution of the barrel calorimeter for photons of energies above 500 MeV is 2%. The central tracking detectors consist of three concentric cylindrical drift chambers that cover the polar angles above 18°. From smallest to largest radii these are: the precision tracking layers detector, the vertex detector (VD), and the main drift chamber. The measurements of the specific ionization energy losses in the outer layers of the main drift chamber and flight times in the TF system provide discrimination between charged particles of different species. All detector subsystems except the muon detectors reside in a uniform axial magnetic field of 1.5 Tesla.

The data sample employed in our analysis corresponds to an integrated e^+e^- luminosity of 2.88 ± 0.03 fb^{-1}. Two thirds of the data was collected at e^+e^- center-of-mass energy of $\sqrt{s} = 2E_b = 10.58$ GeV, the remainder at 10.52 GeV.

B. Trigger System

The CLEO II detector has a three-level hardware trigger system [52] followed by a software filter. The fastest, "zeroth" level (L0) trigger can be either track-based (using the VD and TF) or energy-based (demanding a minimum energy deposition of about 500 MeV in the CsI calorimeter). The calorimeter L0 information develops slowly, so it only comes into effect if the track-based L0 trigger fails; in such cases the tracking information is lost.

The first level (L1) trigger uses track-based information from the VD, TF, and main drift chamber; tracks of transverse momenta in excess of about 340 MeV/c are identified by either of two independent track processors employed in the trigger decisions. Calorimeter information is also utilized at L1. High threshold bits, designed to be set by showering particles, have a threshold of about 500 MeV; low threshold bits, designed to trigger on minimum ionizing particles, have a threshold of about 100 MeV. To trigger at L1 on two low-energy clusters, they must be well-separated in space.

More detailed information from the VD and main drift chamber is used in the second level (L2) trigger. The requirements and accessed momentum range varied between data subsets, but are all modeled in our detector simulations. The software filter (LVL3) is optimized to suppress backgrounds from interactions of the beams with residual gas and vacuum chamber walls. Events which pass LVL3 are recorded. In addition, every eighth event that fails LVL3 is also recorded to allow the LVL3 efficiency to be studied.

The efficiencies of the various trigger components have been measured using data collected with independent or partially independent simultaneous trigger requirements and are incorporated in the detector simulations [1,53,54]. The simulations are carefully run to match the integrated luminosity associated with each trigger configuration. This is necessary because exact trigger requirements in CLEO II have been changed over time to improve the trigger efficiency for events of low particle multiplicities.

C. Monte Carlo Simulation

In our analysis we use a two-photon Monte Carlo (MC) simulation program [55] that is based on the BGMS formalism [2]. The $\gamma^*\gamma^* \to \mathcal{R}$ transition form factors are approximated by:

$$\begin{aligned} |\mathcal{F}_{\gamma^*\gamma^*\mathcal{R}}(Q^2,q^2)|^2 &= |\mathcal{F}_{\gamma^*\gamma\mathcal{R}}(Q^2)|^2 \, \frac{1}{(1+q^2/\Lambda_{\mathcal{R}}^2)^2} \\ &= \frac{1}{(4\pi\alpha)^2} \, \frac{64\pi\Gamma(\mathcal{R}\to\gamma\gamma)}{M_{\mathcal{R}}^3} \, \frac{1}{(1+Q^2/\Lambda_{\mathcal{R}}^2)^2} \, \frac{1}{(1+q^2/\Lambda_{\mathcal{R}}^2)^2} \, , \end{aligned} \tag{8}$$

where Q^2 and q^2 are the absolute values of the squared four-momenta carried by the space-like photons. The pole-mass parameter $\Lambda_{\mathcal{R}} = 770$ MeV has been chosen to approximate the momentum transfer dependence of the form factors. It should be noted that while we have chosen this parameter to be practically the ρ^0 mass, as predicted by the Vector Meson Dominance (VMD) model [56], the pole-mass behavior of the transition form factors $\mathcal{F}_{\gamma^*\gamma\mathcal{R}}$ and the value of the parameter $\Lambda_{\mathcal{R}}$ in the range between 700 and 900 MeV are indicated by various theoretical predictions [13,57] that are not based on VMD. Notice that in the approximation given by Eqn. 8 we assume a factorization of the form factor into the q^2- and Q^2-dependent parts [58]. In the same two-photon simulation program we also generate the decays of the produced mesons. To account for the relativistic effects, helicity conservation, and presence of spin-one particles we simulate the decay chain $\eta' \to \rho^0\gamma \to \pi^+\pi^-\gamma$ according to:

$$\frac{d^2\Gamma(\eta' \to \rho^0\gamma \to \pi^+\pi^-\gamma)}{d\cos\theta^*\, dm_{\pi\pi}^2} \propto \sin^2\theta^* \, \frac{E_\gamma^3}{m_{\pi\pi}} \, \frac{m_\rho \Gamma(m_{\pi\pi})}{(m_\rho^2 - m_{\pi\pi}^2)^2 + m_\rho^2\Gamma^2(m_{\pi\pi})}, \tag{9}$$

with the energy-dependent width, $\Gamma(m_{\pi\pi})$, parameterized by:

$$\Gamma(m_{\pi\pi}) = \Gamma(m_\rho) \, \frac{|\vec{p_a}|^3}{|\vec{p_n}|^3}, \tag{10}$$

where θ^* is the angle between the directions of one of the charged pions and the signal photon, E_γ is the energy of the photon, $\Gamma(m_\rho) = 151$ MeV and $m_\rho = 768$ MeV/c^2 are the nominal width and mass of ρ^0 [59], $m_{\pi\pi}$ is the actual mass of ρ^0, and $|\vec{p_a}|$ and $|\vec{p_n}|$ are the magnitudes of the charged-pion momenta for the actual and nominal masses of ρ^0, respectively. The charged-pion momenta and the angle θ^* are defined in the center-of-mass frame of ρ^0 and the energy of the photon is defined in the center-of-mass frame of η'.

The transport of the generated MC particles through the CLEO II detector is performed by a GEANT-based [60] detector simulation program. The generated events are then processed by the event reconstruction program which also "simulates" random electronic noise and beam-related spurious energy clusters by adding hits from random-trigger data samples into the MC events.

III. ANALYSES OF SINGLE-TAGGED $\gamma\gamma$ FINAL STATES

A. Trigger

The single-tagged two-photon reactions $e^+e^- \to e^+e^-\pi^0$ and $e^+e^- \to e^+e^-\eta$ followed by the decays $\pi^0\to\gamma\gamma$ and $\eta\to\gamma\gamma$ are recorded using either a track-based or an energy-based L0 trigger. The track-based L0 trigger is satisfied when the scattered electron passes through the VD and enters the endcap TF. For tags that scatter at polar angles above 24.5°, thus passing through the entire VD volume, the efficiency of this trigger is about 80% and is determined by the size of the wire-chamber drift cells compared to the time allowed to make the L0 decision. At smaller polar angles we rely on the energy-based L0 trigger. The efficiency of this trigger is 98% (100%) for electrons which deposit 1.0 GeV (more than 1.6 GeV) of energy in the calorimeter.

The L1 trigger is satisfied when at least two clusters, each of energy above 500 MeV, are detected in the calorimeter, with one in the barrel region and the other in one of the endcap regions. There are no L2 requirements for events passing the L0 and L1 trigger conditions described above.

To be recorded, events must fulfill the transverse-momentum requirement of the LVL3 filter that assigns momenta to all calorimeter clusters assuming that they are photons produced at the primary interaction point in the geometrical center of the CLEO II detector. This LVL3 criterion rejects events if the net vector momentum has a component normal to the beam axis in excess of 0.7 GeV/c (1.4 GeV/c) when the total energy detected in the calorimeter is larger than 1.0 (5.0) GeV.

B. Analysis Procedure

In the first part of this section we describe the event selection criteria based on the event topology for the signal production processes. In the second part we explain selection criteria aimed at the suppression of random background. In the third part we discuss the event quality requirements designed to isolate signal events with large uncertainty in the detection efficiency. Finally, in the last part of this section we show the invariant mass spectra for data events that fulfill all selection criteria.

1. Basic Selection Criteria

The event selection criteria for single-tagged $\gamma\gamma$ final states are designed to isolate two-photon events for which the trigger efficiency is high and in which the only missing particle is the untagged electron of high momentum. These events are characterized by the high-energy shower produced by the tag in the endcap calorimeter and two electromagnetic showers of total energy larger than 1 GeV produced by the photons in the barrel calorimeter.

We select events in which three or four energy clusters and no more than one charged track have been reconstructed. The energy of each barrel (endcap) cluster must be larger than 30 (50) MeV. The most energetic cluster is assumed to be produced by the tag and must be in the endcap calorimeter. If a charged track is found, its projected intersection point with the calorimeter must agree with the tag's shower position within 20° as estimated at the primary interaction point. The position of each shower is determined from the energy-weighted average of the centers of the crystals forming this shower. To provide an efficient trigger, the energy of the tag candidate detected in the calorimeter should be above 1.0 GeV (at a later stage of the analysis procedure this cut will be superseded by a tighter requirement). Out of the remaining energy clusters, the two most energetic must be found in the barrel calorimeter at polar angles above 45° (*i.e.*, excluding calorimeter edges), and are assumed to have come from the π^0 or η decays. The fourth energy cluster, if found, should contain less than 200 MeV of energy; the efficiency loss due to this requirement is less than 0.25%. Events with this additional energy cluster may be either signal or beam-gas events with a beam-related noise cluster or partially reconstructed background events of higher particle multiplicities that mimic single-tagged π^0 or η production. By allowing an extra energy cluster, we reduce the uncertainty in the signal efficiency while providing the opportunity for background estimates. A tighter cut on the energy of an additional cluster would make our results more sensitive to the modelling of the noise-related energy clusters and a looser cut on this extra energy would not adequately discriminate against signal-like background which is due to partially reconstructed events.

The overall efficiencies of the basic selection criteria described above are 38% and 30% for the π^0 and η analyses, respectively. These estimates have been obtained using MC signal events generated in the Q^2 range between 1.5 and 9 GeV^2.

2. Background Suppression

The background conditions in two-photon events of low particle multiplicities with tags detected at large and (relatively) small polar angles are different. To provide an adequate background suppression for both regions of polar angle, we separate signal event candidates into two samples that have undergone different experimental cuts. In this subsection we describe this event separation, the sources of random background and the event selection criteria applied to each sample to suppress random background.

When the scattering angle of the tag is larger than 24.5° (as determined from the calorimeter) we select events that have been triggered by the track-based L0 trigger. In addition, we require that these events have exactly one reconstructed charged track consistent with the tag's shower. There is no efficiency loss associated with the tracking requirement which discriminates against background arising mainly from radiative Bhabha events accompanied by photon conversion or bremsstrahlung. We include these events in the track-tagged sample. When the scattering angle is less than 24.5° we accept both track- and energy-based L0 triggers and do not require the presence of the tag's track, because the efficiencies of the track-based L0 trigger and track reconstruction vanish for tags detected in this region of polar angles. We include these events that have been triggered either by the track-based or energy-based L0 trigger in the energy-tagged sample. Notice that while the events from the track-tagged sample must be track-triggered, the events from the energy-tagged sample could be either track- or energy-triggered. Tracking information for events from the track-tagged sample is utilized in background estimates. The track reconstruction efficiency for energy-triggered events is zero.

Before imposing further selection criteria we obtain improved estimates of the tag energy and direction by using transverse-momentum balance and the tag coordinates in the calorimeter. The transverse momenta of the tag and of the photon pair should be nearly identical for signal events because the untagged electron usually carries very little transverse momentum (below 5 MeV/c) according to the prediction of the MC simulation. Since the transverse momentum of the photon pair is measured with much better precision than that of the tag, we equate the magnitude of the transverse momentum of the tag with that of the signal photon pair. To calculate the direction of the tag we require that its trajectory in the magnetic field goes through the center of the tag's shower. To estimate the center of the shower we use the measurement from the calorimeter when the shower is found at polar angles larger than 16.5°. At smaller polar angles, however, we use the geometrical center of the crystal with the largest detected energy. This is necessary in order to reduce the discrepancies between the data and MC simulation. Using the estimates of the tag energy and direction obtained from the transverse-momentum balance we estimate the missing energy and the magnitude of missing momentum. To suppress the background from partially reconstructed events we select events where the discrepancy between the missing energy and missing momentum is less than 2.3 GeV. This cut is 98% efficient for our signal. We note that at a later stage of the analysis procedure we will obtain more precise estimates of the tag energy and direction.

Not only should the magnitudes of the transverse momenta of the tag and the photon pair be nearly equal, their directions are expected to be practically opposite in the plane perpendicular to the beam collision axis. We use the acoplanarity angle, which is the deviation from this expectation, to suppress the background arising from radiative Bhabha events with bremsstrahlung photons produced in the materials of the detector. An event of this origin enters the energy-tagged sample when the track-based L0 trigger is inefficient and a track associated with an electron which radiated in the barrel part of the detector cannot be reconstructed. While for signal events the acoplanarity distribution peaks near zero, for background events it peaks around 12° for the CLEO geometry and CESR kinematics. Acoplanarity discriminates between signal and background events because the measured angular position of the shower created by the electron that has undergone bremsstrahlung is shifted with respect to its direction at the primary interaction point. This shift is due to the bending of the electron track in the magnetic field. To suppress this random QED background in the energy-tagged sample, we select events with acoplanarity less than 5°. The background rejection power of this cut exceeds 10, while efficiency loss varies between 20% and 10% for Q^2 between 1.5 and 2.5 GeV^2. For Q^2 larger than 2.5 GeV^2 the efficiency of the acoplanarity cut for the energy-tagged events is 90%. In contrast to the energy-tagged sample, the track-tagged sample contains very few bremsstrahlung-accompanied radiative Bhabha events because each of these background events has an additional charged track and does not pass basic selection criteria (the track reconstruction efficiency for high-energy electrons detected in the barrel part of the detector is practically 100% for events recorded by the track-based L0 trigger). We select the track-tagged events with acoplanarity less than 15°. The efficiency of this loose cut on acoplanarity is 99%.

We use the decay angle θ_d to further suppress background arising from radiative Bhabha events accompanied by low-energy split-off clusters. The decay angle is determined from the directions of the π^0 (or η) candidate in the lab frame and one of the daughter photons in the center-of-mass frame of π^0 (or η). Simulation of the detector acceptance predicts that the distribution of $|\cos\theta_d|$ is flat between 0.0 to 0.95 and decreases rapidly beyond 0.95 due to the acceptance loss for soft photons. In contrast to the signal, radiative Bhabha events with split-off clusters congregate at $|\cos\theta_d| = 1.0$ because these clusters typically are of low-energy. We reject these asymmetric decays by requiring $|\cos\theta_d| < 0.90$.

The acoplanarity and decay angle cuts do not eliminate random background completely, because radiative Bhabha events accompanied by γ conversions in detector materials look similar to signal events when triggered by the energy-based L0 trigger. However, we have found that the shape of this background is monotonic within the signal and sideband regions of the $\gamma\gamma$ invariant mass distribution in both analyses.

3. Event Quality Requirements

The angular spectrum of the scattered electrons peaks sharply at small polar angles due to the kinematics of processes studied in our analyses. Thus, to measure the cross sections for two-photon production in a tagged mode we must understand this critical region of our experimental apparatus very well. While we can, in principle, detect tags at polar angles as small as 13°, the fraction of the tag energy collected in the calorimeter at these small polar angles is usually less than 20% and might be insufficient to trigger an event. In addition, even if the trigger is satisfied, an event might be rejected by the LVL3 filter, which is biased against events with large net transverse momenta. To select events identified in the detector regions where the trigger and LVL3 efficiencies are well understood, we need better estimates of the tag energy and scattering angle.

To make precise estimates of the tag energy and scattering angle we use energy-momentum conservation assuming that the only particle missing detection is the untagged electron with zero transverse momentum. In practice, this method allows us to estimate the parameters of the tag when we measure only the four-momentum of the hadronic system and assume that we know the charge of the untagged electron (from crude measurement of the direction of missing momentum). From conservation laws we estimate the tag energy E with an r.m.s. resolution of 0.003 E and the scattering angle with an r.m.s. resolution of better than 0.6°. In addition, to estimate the scattering angle for track-tagged events we use the polar angle of the reconstructed charged track associated with the tag. By using the polar angle of the track we achieve an additional small improvement in the resolution of the scattering angle for these events. The tag energy for track-tagged events, however, is estimated from energy-momentum conservation; *i.e.* no tracking information is used to estimate the tag energy. In further discussions the values of the tag's parameters estimated from energy-momentum conservation and the polar angle of the charged track are referred to as constrained values of the tag energy and scattering angle. In Fig. 1 we show the resolution functions of the tag energy and scattering angle determined from the differences between analyzed (*i.e.* measured or constrained) and generated quantities (normalized to the generated value for the energy resolution function). These resolution functions have been obtained using simulated π^0 events which have values of Q^2 between 1.5 and 9 GeV^2 and satisfy all selection criteria discussed above. In our analyses we estimate Q^2 for each event using constrained values of the tag energy and scattering angle. This results in an r.m.s. Q^2 resolution that varies between 0.1 and 0.3 GeV^2 for the Q^2 region between 1.5 and 9 GeV^2.

To isolate the detector region for which the efficiency is small and poorly understood, events with constrained values of the tag scattering angle less than 15° are rejected from further analysis. In addition, to reduce the systematic uncertainty in the efficiency of the LVL3 filter we select events in which the detected fraction of the tag energy is at least 50%. This fraction is estimated from the calorimeter measurement and the constrained value of the tag energy. The efficiency of this fractional tag-energy cut is 90% for tags which scatter at 15° and is practically 100% for tags which scatter at angles larger than 19°. We have measured the dependence of this efficiency on the polar angle using radiative Bhabha events triggered inclusively by the barrel TF-based L0 trigger. We show the efficiency of the fractional tag-energy cut in Fig. 2.

4. Event Selection Results

In Figs. 3 and 4 we show the $\gamma\gamma$ invariant mass distributions for data events that pass all selection criteria for the π^0 and η candidates and have values of Q^2 between 1.5 and 9 GeV^2. The points with error bars in these figures represent event yields in data. The solid line in each figure shows the result of the binned likelihood fit to data with the signal line shape obtained from the MC simulation and an approximation of the remaining random background. In the $\pi^0 \to \gamma\gamma$ analysis, the background arising from radiative Bhabha events accompanied by photon conversions is approximated by an exponential. In the $\eta \to \gamma\gamma$ analysis random background is approximated by the sum of an exponential and a constant because the $\gamma\gamma$-mass distribution shown in Fig. 4 contains two major background components. While the first component has the same source as in the π^0 analysis, the second component is due to radiative Bhabha events with bremsstrahlung radiation in the interface between the drift chambers.

C. Background Estimates

The data may contain π^0 and η events that are due to beam-gas interactions or partially reconstructed events of higher particle multiplicities. To estimate the beam-gas contribution we use the distributions of the event vertex position, visible energy and squared missing mass. Given the profile of the residual gas density near the beam-collision point, the vertex position of beam-gas events is much more diffuse than that of the signal. In addition, while beam-gas events should have visible energy (*i.e.*, total energy detected in the calorimeter) less than the beam energy, most events from the track-tagged sample have visible energy larger than the beam energy. However, at small scattering angles the tag needs to go through a larger amount of the detector materials than at large scattering angles and can lose a significant part of its energy before reaching the calorimeter. As a result, a large fraction of events from the energy-tagged sample (about 20%) falls into the visible energy region below the beam energy. For these energy-tagged events we have studied the distribution of the squared missing mass estimated assuming the electroproduction hypothesis $e^{\pm}p \to e^{\pm}p\pi^0$(or η). Using the discriminating power of the distributions described above we conclude that the beam-gas background is very small and warrants no subtraction.

To estimate the background contribution to the track-tagged sample due to e^+e^- annihilation we have studied the correlation between the charge and the direction of the tag's track. Signal processes should produce virtually all positrons in the $+z$ hemisphere and electrons in $-z$ hemisphere, where $+z$ is the direction of the positron beam. However, e^+e^- annihilation should produce practically the same number of electrons (and positrons) in both z-hemispheres. We do not observe a single data event in which this charge-direction correlation indicates e^+e^- annihilation processes. We conclude that the background from e^+e^- annihilation is fewer than 1 event in both track- and energy-tagged samples because the angular distribution of the electrons from this background source is expected to be relatively uniform (compared to the rapidly changing signal).

Finally, there may be some background from other single-tagged two-photon processes. The process $e^+e^- \to e^+e^- f_2(1270)$ followed by the decay $f_2(1270) \to \pi^0\pi^0$ is the most likely source of the feed-down for the $\pi^0 \to \gamma\gamma$ analysis. To estimate the feed-down from this process, we remove the cut on the energy of the fourth, least energetic cluster and repeat the analysis. We estimate that out of 1300 π^0 event candidates in data, 80 ± 40 events are due to the feed-down, where the error reflects the uncertainty of our method. This uncertainty arises from the fact that the π^0 misidentification probability for the feed-down from the decay $f_2(1270) \to \pi^0\pi^0$ depends on the relative strengths of the couplings between the tensor meson and two space-like photons of various total helicity (determined in the center-of-mass frame of $f_2(1270)$). The central value of the background estimate quoted above has been derived assuming that the $f_2(1270)$ production proceeds exclusively via the helicity ± 2 channel. The error reflects the uncertainty in the background estimate which becomes larger (smaller) when we assume that $f_2(1270)$ is produced only in the helicity 0 (± 1) state. We assign this large error to the background estimate because the contributions of different helicity amplitudes to the single-tagged cross section for this background process have not been measured yet. We observe the $f_2(1270)$ feed-down at Q^2 below 4 GeV^2 and subtract its contribution to each Q^2 interval using the shapes of the energy spectra of an additional cluster measured from data and signal MC simulation. We do not observe a feed-down in the $\eta \to \gamma\gamma$ analysis. We have also studied the feed-down from single-tagged two-photon processes of higher final-state particle multiplicities such as the production of η and η' and estimate the overall contribution from these background processes to be insignificant in both analyses.

D. Systematics

Contributions to the systematic errors arise from four sources. The primary uncertainty is due to systematic biases in the determination of the event selection efficiency. These biases are detailed below. The second contribution is a 1% systematic error on integrated luminosity [61]. This error is based on estimates of the theoretical uncertainties in the QED radiative corrections in the MC event generators for the processes $e^+e^- \to e^+e^-$ and $e^+e^- \to \gamma\gamma$ which are employed in the determination of integrated luminosity. The third contribution is a 1% systematic error due to the background estimation procedure. The fourth source of systematic error is due to small uncertainties in the branching fractions for studied decay chains. This error is negligible in the $\pi^0 \to \gamma\gamma$ analysis and is less than 1% in the $\eta \to \gamma\gamma$ analysis.

The largest systematic error is due to the fractional tag-energy cut. We have measured the efficiency of this cut using radiative Bhabha events in data. The relative statistical error in this efficiency is less than 3% for polar angles larger than 15° so we conservatively include a 3% error to the systematics of energy-tagged events. Note that the fractional tag-energy cut is fully efficient for track-tagged events, so no contribution is made to their systematics.

The efficiency of the LVL3 filter has been measured using π^0 signal data events that would have normally been discarded by this filter. The statistical error in the measured efficiency is 2% and this gives an estimate of the systematic error.

The next error comes from the uncertainty in the photon reconstruction efficiency. We have determined this uncertainty to be 2%, or 1% per photon from a global fit of the measured ratios of the η and η' branching fractions to their average values [59].

We have measured the efficiency of the VD L0 trigger over the entire data sample using the TF-triggered endcap Bhabha events and have found that this efficiency varies by up to 2.5% of its central value between data subsets. In our analysis we use the average value for the VD L0 trigger efficiency of 80% and include its r.m.s. variation of 2% to the systematic error for track-tagged events.

To estimate the systematic uncertainty in the efficiency of the extra energy cut we have utilized the shape of the extra energy distribution measured from signal data in the $\eta' \to 6\gamma$ analysis. We estimate this uncertainty to be 2%.

The efficiency of the acoplanarity cut for energy-tagged events is between 80% and 90%, depending on Q^2. To estimate the uncertainty in this cut, we have measured its efficiency assuming that the detector simulation systematically underestimates or overestimates azimuthal angular positions of all showers and the tag in the calorimeter by one standard deviation of the angular resolution function. We find that under these conditions the efficiency varies by less than 1% of itself in any Q^2 interval. We include this value of 1% to the systematics of energy-tagged events.

We have also studied other sources of uncertainties such as the efficiencies of missing energy-momentum and decay angle cuts and conclude that their total contribution to the systematics is insignificant.

We include the systematic uncertainties in the amount of feed-down background and in the shape of the $\gamma\gamma$-mass spectrum for random background to the statistical error on the number of signal events in each Q^2 interval. These errors are between 1% and 5% being larger at smaller Q^2.

While the acoplanarity and fractional tag-energy cuts affect only energy-tagged events, the track-based L0 trigger is specific for the track-tagged events. Thus, the systematic uncertainties associated with the two event samples are different. To estimate the systematics for each Q^2 interval we have used the Q^2 distributions for MC events which belong to the energy- and track-tagged samples. We show these distributions in Fig. 5.

Our analyses should not be significantly affected by the QED radiative corrections. To order α^5, in addition to the vacuum polarization and one virtual photon exchange, these corrections describe the processes $e^+e^- \to e^+e^-\mathcal{R}\gamma$, where $\mathcal{R}$ is one of the studied pseudoscalar mesons [62]. When a radiative photon carries away part of the initial center-of-mass energy and remains undetected, we use the nominal value of the beam energy before the radiation and overestimate Q^2 according to Eqn. 2. However, when we estimate the tag energy and scattering angle from energy-momentum conservation, we underestimate Q^2. Both distortions described above are small effects because the energy spectrum of radiative photons is very soft. We neglect the effect of the QED radiative corrections on the smearing of the Q^2 spectrum because these two small effects largely cancel each other. The net smearing is such that in our analysis procedure the measured cross sections are insignificantly underestimated.

There is another aspect of the QED radiative corrections that might need to be taken into account. Namely, when we unfold the differential cross sections and obtain the transition form factors, we rely on the prediction of a numerical integration that does not contain these corrections and underestimates the cross sections. We expect the QED radiative corrections to the cross sections for single-tagged events to be smaller than 2.4% [62,63] and this gives a 1.2% estimate of the systematic uncertainty introduced in the values of $\mathcal{F}_{\gamma^*\gamma\mathcal{R}}$ from the unfolding procedure[8]. Finally, we should emphasize that in order to account for the QED radiative corrections in a consistent manner we should have had these corrections implemented in the MC event generator that we use to measure the detection efficiency. We did not use such an event generator in our analysis.

The efficiencies of the event selection criteria employed in our analysis are not flat over the studied Q^2 region. Most systematic errors for these efficiencies are quoted for a region of low Q^2 (*i.e.* less than 3 GeV^2) where the efficiencies are smaller and the systematic uncertainties are larger than at high Q^2 (above 3 GeV^2). These estimates are conservative in the high Q^2 region where a small fraction of signal events has been detected.

In the analyses of $\gamma\gamma$ final states the systematic errors contribute a 5% uncertainty to the measured cross sections. As we described above, this uncertainty includes a contribution of $\sim 3\%$ that comes from different sources for energy- and track-tagged event samples.

[8]If we include the corrections that are due to the vacuum polarization of the probe (*i.e.* highly virtual) photon in the definition of the measured form factors, the remaining QED radiative corrections to these form factors would be smaller than 0.5%. The vacuum polarization and all other corrections are of opposite signs and partially cancel each other.

IV. ANALYSES OF SINGLE-TAGGED 6γ AND 10γ FINAL STATES

The following subsections mainly describe the differences among the analyses of 6γ and 10γ final states and the previously described analyses of 2γ final states, since they share many common features.

A. Trigger and Analysis Procedure

In addition to the trigger utilized for $\gamma\gamma$ final states, 6γ and 10γ single-tagged events have been collected with a modified energy-based L1 trigger, which is fulfilled when the high energy shower associated with the tag candidate is found in the endcap calorimeter and two well-separated clusters, each of detected energy above 100 MeV, are identified in the barrel calorimeter. This additional trigger option is especially important for $3\pi^0 \to 6\gamma$ and $5\pi^0 \to 10\gamma$ final states because few of the photons resulting from the π^0 decays have sufficient energy to satisfy the high-energy trigger threshold of about 500 MeV.

Each event candidate should contain a tag (in the endcap part of the calorimeter), six, seven, ten or eleven photon candidates, and no charged tracks except the tag's track, if reconstructed. The efficiencies of these basic selection requirements are 30%, 31% and 12% for the $\eta \to 6\gamma$, $\eta' \to 6\gamma$, and $\eta' \to 10\gamma$ analyses, respectively, with the reconstruction efficiency of about 80% per photon being the dominant source.

To reduce the systematic uncertainty in the trigger efficiency we select events with the most energetic photon candidate detected in the barrel calorimeter at polar angles above 37°. The trigger efficiency for these events is larger than 90%. We apply the same missing energy-momentum cut of 2.3 GeV as in the $\gamma\gamma$ analyses. We require acoplanarity less than 30° and do not apply a decay angle cut because there is no need to suppress the small background due to radiative Bhabha events.

Only events that contain at least one combination of the required number of $\pi^0 \to \gamma\gamma$ and $\eta \to \gamma\gamma$ candidates are accepted for further analysis. To give an example, we consider the decay chain $\eta \to 3\pi^0 \to 6\gamma$. Among six or seven photon candidates, there must be at least one set of three π^0 candidates, where each π^0 candidate is identified within $[-9.0,\ 3.5]\sigma$ of the nominal π^0 mass. The mass resolution σ has been measured as a function of energy and polar angle from data, with a typical value between 6 and 8 MeV/c^2. If there is more than one way to form three π^0 candidates, we use the best combination, *i.e.* the one which has the smallest χ^2, where

$$\chi^2 = \sum_{i=1}^{3} \frac{(M^i_{\gamma\gamma} - M_{\pi^0})^2}{\sigma_i^2}. \tag{11}$$

We follow the same procedure for 6γ and 10γ final states in which we search for the best $\pi^0\pi^0\eta$ and $5\pi^0$ combinations, respectively. To obtain a better estimate of the parent particle four-momentum we perform a kinematic fit for each $\gamma\gamma$-decay candidate from the best combination. For events in which we find an additional energy cluster that has not been used to form any of the π^0 or η candidates, we require that the energy of this cluster be less than 200 MeV. In contrast to the $\gamma\gamma$ analysis, this energy cluster is not necessarily the least energetic one.

Events that are accepted for further analysis must have constrained values of the tag scattering angle larger than 15°. In addition, the detected fraction of the tag energy must be at least 50%. To estimate the constrained values of the tag energy and scattering angle we employ energy and momentum conservation laws in which we use the four-momenta of the reconstructed $\pi^0 \to \gamma\gamma$ and $\eta \to \gamma\gamma$ candidates obtained from the kinematic fits.

In Figs. 6–8 we show the invariant mass distributions for data events that pass all selection criteria for the η and η' candidates and have values of Q^2 between 1.5 and 9 GeV^2. The points with error bars in these figures represent event yields in data. The solid line in each figure shows the result of the binned likelihood fit to data with the signal line shape obtained from the MC simulation and a first-order polynomial chosen to approximate the remaining random background.

B. Background Estimates and Systematics

To estimate the feed-down background, we have studied the distribution of extra energy when the cut on this quantity has been removed. We conclude that out of 187 event candidates for the decay $\eta \to 3\pi^0$ in data, 7 events are due to feed-down from the decay chain $\eta' \to \pi^0\pi^0\eta \to 5\pi^0$. To subtract this feed-down background, we use the extra energy spectra measured from data and signal MC simulation. We do not observe a feed-down in the η' analyses. We estimate the beam-gas and e^+e^- annihilation backgrounds to be less than 1% of the signal in each analysis.

In the analyses of 6γ and 10γ final states we include a 1% error to the systematics due to the uncertainty in the efficiency of the barrel energy-based L1 trigger. To estimate this uncertainty we have studied the efficiency of a low-energy trigger threshold for signal data and MC events which have been inclusively triggered with a high-energy trigger threshold. All other systematic uncertainties have been discussed in Section III.D.

In the analyses of 6γ and 10γ final states the overall systematic uncertainties in the measured cross sections are 7% and 11%, respectively.

V. ANALYSES OF SINGLE-TAGGED FINAL STATES WITH CHARGED PIONS

In this section we describe the analyses of final states that contain the tag, two or four charged pions, and at least one photon.

A. Trigger

As we described in preceding sections, charged tracks can be reconstructed only in events which have been recorded with the track-based L0 trigger. This trigger is satisfied by two well-separated TF hits, or one TF hit and a VD track. The L0 triggers are not correlated with the L1 triggers; when any of the L0 triggers is satisfied, all L1 triggers are examined [52].

In addition to the energy-based L1 trigger described previously, there are several track-based L1 triggers which are efficient for events with charged particles:

- The L1 "electron" trigger is satisfied by a high-threshold bit in the barrel calorimeter and a charged track penetrating more than halfway through the volume of the main drift chamber.
- The L1 "two-track" trigger is efficient for events with two or more low transverse-momentum charged particles; it requires at least two hits in either region of the TF system, two well-separated low-threshold clusters in the barrel calorimeter, and two charged tracks, each of transverse momentum above 90 MeV/c. The L2 trigger is fulfilled when at least one charged track of transverse momentum larger than 340 MeV/c is identified.
- The "hadronic" triggers are designed for multi-particle final states from e^+e^- annihilation, but have significant efficiency for this analysis as well. These have a variety of possible criteria involving the drift chambers, TF, and low-threshold bits of the calorimeter. In general, at least three tracks are required.

Associated with these track-based L1 triggers, earlier data sets had a L2 requirement of a VD hit pattern consistent with a charged track of transverse momentum larger than 125 MeV/c. The LVL3 filter does not reject events that are collected by the track-based L1 triggers.

B. Analysis Procedure

Each event candidate must contain the tag, an exact number of charged tracks (excluding the tag's track, if reconstructed), and at least as many photon candidates as are needed for full reconstruction of a studied decay chain. All tracks except for the tag's track are assumed to be due to charged pions. The net charge of the reconstructed pions must be zero. Photon candidates include all barrel (endcap) calorimeter clusters of energies larger than 30 (50) MeV except for those that are closest to the intersection points of charged tracks with the calorimeter. The efficiencies of the basic requirements described above are defined by the charged pion and photon reconstruction efficiencies, each about 80% per particle.

To select events that trigger with high efficiency and small systematic uncertainty, we impose several event-quality criteria. Namely, we require that at least one charged track of transverse momentum larger than 250 MeV/c be detected. In addition, the charged track of largest transverse momentum and either the tag or the most energetic photon candidate must be detected in the barrel calorimeter at polar angles above 37°. Finally, we reject events which contain charged tracks of momenta less than 80 MeV/c because for these tracks the systematic uncertainty in the track reconstruction efficiency is large.

Given that $\rho^0\gamma$ events are primarily recorded with the energy-based L1 trigger, tighter event selection criteria are imposed in this analysis. We select events which have at least one charged track of transverse momentum above 450 MeV/c. The most energetic photon candidate must have energy, E_γ, larger than 130 MeV. We assume this photon candidate to be due to the signal process $\eta' \to \rho^0\gamma$. To suppress random background we select events with the reconstructed $\pi^+\pi^-$ mass between 550 and 800 MeV/c^2. This is referred to as the ρ^0-mass cut.

In the analyses of the final states that contain the decays $\pi^0 \to \gamma\gamma$ and $\eta \to \gamma\gamma$, events must contain at least one combination of the exact number of the candidates for these decays as required for full reconstruction of the studied decay chain. The energy clusters that enter the best combination are assumed to be signal photons. The total energy collected in the calorimeter clusters other than the signal photon candidates and the energy clusters matched to the projections of the charged tracks must be less than 500 MeV. These extra energy clusters are mostly due to the interactions of the charged pions with the materials of the detector. No requirement is made on the number of such clusters.

We use the momenta of the charged tracks and signal photons (after kinematic fits, where applicable) and employ energy-momentum conservation to estimate the tag energy and scattering angle. We select events in which the detected fraction of the tag energy is at least 50% and a scattering angle is larger than 15° where both parameters are estimated using energy-momentum conservation.

In the $\eta \to \pi^+\pi^-\pi^0$ analysis we need to suppress a large feed-down from the decay chain $\eta' \to \pi^0\pi^0\eta \to \pi^+\pi^-3\pi^0$. To suppress this feed-down, we require the difference between the measured and constrained values of the tag scattering angle be less than 2°. The feed-down suppression power of the combination of this and the extra energy cuts is a factor of 23, while the efficiency loss is less than 3%.

We employ the particle identification capabilities of our apparatus to reduce the large random background observed in the $\eta' \to \rho^0\gamma$ analysis. This random background is primarily due to the process $e^+e^- \to e^+e^-e^+e^-$ accompanied by bremsstrahlung radiation, split-off showers or beam-related energy clusters. To suppress random background we utilize the fact that specific ionization energy losses, dE/dx, are larger for electrons than for charged pions. This information is used in the requirement on P_{χ^2}, the upper tail probability of the χ^2 distribution of the dE/dx measurements for charged pion candidates [64]. In the ideal case (*i.e.* if the dE/dx distribution were Gaussian) the correct choice of the particle-identification hypothesis would produce a uniform P_{χ^2} distribution, while events with an incorrect particle-identification hypothesis tend to congregate near zero. We calculate P_{χ^2} for the tracks assuming them to be due to charged pions. To suppress unwanted background events, P_{χ^2} is required to be larger than 0.005. The efficiency of the P_{χ^2} cut is not 99.5% but 98% because a small fraction of the signal events (in both data and simulation) does not have dE/dx information and the dE/dx distribution has non-Gaussian tails. The same cut on P_{χ^2} is applied in all analyses with charged pions.

In Figs. 9–13 we show the invariant mass distributions for data events that pass all selection criteria for the η (η') candidates and have values of Q^2 between 1.5 and 20 (30) GeV^2. The points with error bars in these figures represent event yields in data. The solid line in each figure shows the result of the binned likelihood fit to data with the signal line shape obtained from the MC simulation and a linear approximation of the remaining random background. The remaining random background observed in the analysis of the $\pi^+\pi^-\gamma$ final state is due to the process $e^+e^- \to e^+e^-\mu^+\mu^-$ accompanied by noise and split-off energy clusters.

C. Background Estimates and Systematics

To estimate the feed-down background, we have analyzed the distributions of extra energy and the difference between the measured and constrained values of the tag scattering angle when the cuts on these quantities have been removed. We conclude that fewer than 2 events in the $\eta \to \pi^+\pi^-\pi^0$ analysis are due to feed-down from the decay chain $\eta' \to \pi^0\pi^0\eta \to \pi^+\pi^-3\pi^0$. We have not identified any feed-down background in the η' analyses. We estimate that the background contribution from beam-gas interactions and e^+e^- annihilation processes is less than 1% of the signal in all analyses. This gives an estimate of the relevant systematic uncertainty.

To estimate the systematic uncertainty in the efficiency of the L0 trigger, we select signal events that are triggered by the TF-based L0 trigger and measure the VD efficiency per event. Using a similar method we measure the efficiency of the TF-based L0 trigger for events that are triggered by the track-based L0 trigger. We estimate the uncertainty in the L0 trigger efficiency to be 1%, which is the typical deviation between either of these efficiencies measured from data and simulation. Note that the efficiency of the L0 trigger is higher than 98% for events which satisfy the basic selection requirements.

We have measured the efficiency of the P_{χ^2} cut in a nearly background-free environment using fitted mass distributions for signal events in data and MC simulation for the decay chain $\eta' \to \pi^+\pi^-\eta \to \pi^+\pi^-2\gamma$. We have found this efficiency to be 98% (as discussed in the previous subsection) and use the 2% statistical error of this measurement as an estimate of the systematic uncertainty.

To estimate the uncertainty in the efficiency of the E_γ cut in the $\eta' \to \rho^0\gamma$ analysis, we have measured this efficiency assuming that the energies of the reconstructed photons in the simulation are systematically shifted by 2% of their nominal values. We have observed a relative change of 1% in the efficiency of the E_γ cut and this gives an estimate of its systematic uncertainty.

We estimate the uncertainty in the track reconstruction efficiency to be 2% per charged pion. It is determined from a global fit of the measured ratios of the η and η' branching fractions to their average values [59].

The uncertainty in the efficiency of the ρ^0-mass cut is negligible because, except for the ρ^0-line shape, the matrix element for the decay chain $\eta' \to \rho^0\gamma \to \pi^+\pi^-\gamma$ is determined by QED and kinematics. To confirm this statement we remove the ρ^0-mass and E_γ cuts and compare the distributions of E_γ and $|\cos\theta^*|$ measured from signal data and MC simulation, where E_γ is the signal photon energy in the lab frame[9]. These distributions are shown in Figs. 14 and 15. We observe good agreement between the data and MC spectra of E_γ and $|\cos\theta^*|$ and conclude that the approximations given by Eqns. 9 and 10 describe the data well. We note that both figures show the observed spectra, *i.e.* no detection efficiency corrections have been applied to these distributions. The good agreement between the shape of the $|\cos\theta^*|$ distribution obtained from the simulation and $\sin^2\theta^*$ curve is due to the detection efficiency being practically flat over the full range of $|\cos\theta^*|$.

All other systematic uncertainties have been discussed in Sections III.D and IV.B. In the analyses of final states with charged pions the overall systematic uncertainty in the measured cross sections is between 7% and 10%, depending on the final state.

VI. UNFOLDING PROCEDURE FOR THE TRANSITION FORM FACTORS

To measure the products of the differential cross sections and branching fractions for each decay chain we use the following analysis procedure. Data events that pass all selection criteria are used to form the Q^2 distribution where the value of Q^2 for each event is estimated from energy-momentum conservation (and the polar angle of the tag's track when the track is reconstructed). Next we divide the event yields into Q^2 intervals. For each Q^2 interval we obtain the number of signal events in data from the fit to the invariant mass distribution. Then we estimate and subtract the feed-down background using the methods described in preceding sections. Finally we correct the background-subtracted number of signal events for the detection efficiency. The signal line shapes used in the fits and the detection efficiencies are determined from the detector simulation for each Q^2 interval.

To extract the transition form factors we compare the measured and the predicted values of the cross sections. Namely, for each Q^2 interval, we measure the form factors $\mathcal{F}^{data}_{\gamma^*\gamma\mathcal{R}}(\tilde{Q}^2)$ from:

$$|\mathcal{F}^{data}_{\gamma^*\gamma\mathcal{R}}(\tilde{Q}^2)|^2 = \frac{\sigma(data)}{\sigma(MC)}|\mathcal{F}^{MC}_{\gamma^*\gamma\mathcal{R}}(\tilde{Q}^2)|^2, \tag{12}$$

where $\mathcal{F}^{MC}_{\gamma^*\gamma\mathcal{R}}(\tilde{Q}^2)$ is the approximation for the Q^2-dependent part of the form factor in MC simulation, and $\sigma(data)$ and $\sigma(MC)$ are the cross sections for this Q^2 interval measured in data and predicted using numerical integration, respectively. The transition form factors are measured at $\tilde{Q}^2$ where the differential cross sections achieve their mean values according to the results of numerical integration. The numerical results have been obtained at an average center-of-mass energy of 10.56 GeV with the approximation for the form factor given by Eqn. 8.

The Q^2 distributions measured from data and obtained numerically are shown in Figs. 16 and 17 for the $\pi^0 \to \gamma\gamma$ and $\eta \to \gamma\gamma$ analyses, respectively. Only statistical errors are shown in these figures. To plot the results of numerical integration we use $\Gamma(\pi^0 \to \gamma\gamma) = 7.74$ eV and $\Gamma(\eta \to \gamma\gamma) = 463$ eV [59].

We show our experimental results in Tables I–X. These tables show the Q^2 intervals, event yields obtained from the fits, numbers of signal events after subtraction of the feed-down background, detection efficiencies, the $\tilde{Q}^2$ values, the products of the differential cross sections and relevant branching fractions, and the transition form factors, represented in the form $\tilde{Q}^2|\mathcal{F}_{\gamma^*\gamma\mathcal{R}}(\tilde{Q}^2)|$. In Tables I–X the first error is statistical and the second error (where given) is systematic.

VII. COMPARISON OF THE RESULTS WITH THEORETICAL PREDICTIONS

In this section we compare the results for π^0 with theoretical predictions. For the transition form factors of η and η' we compare the results with the PQCD asymptotic prediction only because little is known in theory about the wave functions of these mesons. No predictions for the form factors of η and η' are available at this time except for the prediction of Kroll *et al.* [13] where these authors assumed that the shapes of the wave functions of all three pseudoscalar mesons are similar.

---

[9]These figures of merit for the analysis of the decay chain $\eta' \to \rho^0\gamma \to \pi^+\pi^-\gamma$ were proposed in [48].

A. Results for π^0

In Figures 18–21 we compare our results for $Q^2|\mathcal{F}_{\gamma^*\gamma\pi^0}(Q^2)|$ with the theoretical predictions. Also shown in these figures are the results of the CELLO experiment [50] and the asymptotic prediction of PQCD given by Eqn. 5. For both experimental results the error bars represent the statistical errors only. To plot the results of the theoretical predictions we use their published analytical forms. To estimate the value of f_π we use Eqns. 4 and 6 and the tabulated two-photon partial width of π^0 [59]. This estimate of f_π (92.3 MeV) agrees with its experimental value (92.4 MeV) which has been measured previously from charged pion decays[10] [59].

In Fig. 18 the results are compared with the predictions made by Jakob *et al.* [13]. These authors calculated the $\gamma^*\gamma \to \mathcal{R}$ transition form factor by employing a PQCD-based technique and QCD radiative corrections [14]. They used two estimates for the π^0 wave function: the asymptotic wave function and the CZ wave function. This theoretical prediction gives a much better agreement with our results when the asymptotic wave function is used. In terms of the PQCD-based approach this indicates that the wave function has already evolved to the asymptotic form at Q^2 as small as 1 GeV^2. Notice that $\mathcal{F}_{\gamma^*\gamma\pi^0}$ calculated with the CZ wave function changes when the QCD evolution of this wave function over the studied Q^2 range is taken into account according to [37]. The transition form factor does not change when the asymptotic wave function is used because this wave function exhibits no QCD evolution to leading order in α_s. However, in next-to-leading order in α_s any wave function, including the asymptotic, is subject to the QCD evolution [65]. If this evolution is taken into account the prediction with the asymptotic wave function which has been derived to leading order in α_s would also change slightly [37].

Cao *et al.* also made a prediction based on PQCD [16]. These authors disagreed with the approximations made to simplify the form of HSA in [13]. Their prediction includes transverse momentum corrections and is compared with our results in Fig. 19 for the asymptotic and CZ wave functions. The theoretical prediction of Cao *et al.* yields a smaller value of $\mathcal{F}_{\gamma^*\gamma\pi^0}$ for Q^2 less than 8 GeV^2 when the CZ wave function is used. This is a most intriguing result because the CZ wave function has been proposed to account for measured excesses in the rates for various processes, thus leading to larger values of the form factors and cross sections [6].

The prediction of Radyushkin *et al.* [57] based on the QCD sum-rules method [11] is compared with the experimental results in Fig. 20. This calculation describes the saturating behavior of our measurement, though it disagrees with the data at smaller Q^2. It should be noted that at low Q^2 the prediction is not expected to agree with the data: the QCD radiative corrections which would be larger at smaller Q^2 have not been included in this theoretical analysis. The discrepancy between the absolute values of the asymptotic limits of PQCD and of this prediction might be due to the uncertainties in the expectation values of the vacuum condensates that are known only with 30% precision [11]. However, according to the authors, the agreement can be achieved by means of complicated QCD-evolution analysis of the correlator functions used in this theoretical approach [33].

Finally, we derive the value of the pole-mass parameter Λ_{π^0} which we use to represent our results in a simple phenomenological form. We fit our results for $|\mathcal{F}_{\gamma^*\gamma\pi^0}(Q^2)|^2$ with a function given by Eqn. 8 and obtain the following result:

$$\Lambda_{\pi^0} = 776 \pm 10 \pm 12 \pm 16 \text{ MeV}, \tag{13}$$

where the first error is statistical, the second error represents systematic uncertainties of our measurements, and the third error is due to the uncertainty in the value of $\Gamma(\pi^0 \to \gamma\gamma)$ [59]. The result of the fit is shown in Fig. 21. While we observe that a simple VMD-like approximation describes the data very well, we should note that it disagrees with the asymptotic prediction of PQCD. Also shown in Fig. 21 is the interpolation given by Eqn. 7.

B. Results for η

We show the results of our measurements for $Q^2|\mathcal{F}_{\gamma^*\gamma\eta}(Q^2)|$ in Fig. 22. This figure also shows the asymptotic prediction of PQCD given by Eqn. 5 and the interpolation given by Eqn. 7. To estimate the value of f_η (97.5 MeV) we use Eqns. 4 and 6 and the tabulated two-photon partial width of η [59]. We fit the $|\mathcal{F}_{\gamma^*\gamma\eta}(Q^2)|^2$ distributions measured using each decay chain with the functional form given by Eqn. 8 and obtain the values of the pole-mass parameter Λ_η that are shown in Table XI. In this table, for each measurement, the first error is statistical, the second error represents systematic uncertainties of our measurement, and the third error reflects the uncertainty in

[10]For each meson $\mathcal{R}$, where $\mathcal{R}$ is π^0, η or η', our definition of the meson decay constant $f_\mathcal{R}$ differs by a factor of $1/\sqrt{2}$ from the one accepted by the Particle Data Group and given in [59].

the two-photon partial width of η. From a simultaneous fit to our three measurements for the production of η we obtain the following value of the pole-mass parameter:

$$\Lambda_{\eta} = 774 \pm 11 \pm 16 \pm 22 \text{ MeV}. \tag{14}$$

The result of this fit is shown in Fig. 22.

We use the measured values of the parameters Λ_{π^0} and Λ_{η} to compare the soft non-perturbative properties of π^0 and η. This is a legitimate comparison because the chiral limit given by Eqn. 6 and the asymptotic prediction given by Eqn. 5 are expected to hold for both π^0 and η. From the comparison between the measured values of Λ_{π^0} and Λ_{η} we conclude that the Q^2 shapes of the $\gamma^*\gamma \to$ meson transition form factors of π^0 and η are nearly identical, which strongly indicates the similarity between the wave functions of these mesons.

C. Results for η'

We show the results of our measurements for $Q^2|\mathcal{F}_{\gamma^*\gamma\eta'}(Q^2)|$ in Fig. 23. This figure also shows what would be the PQCD asymptotic prediction given by Eqn. 5 for $Q^2|\mathcal{F}_{\gamma^*\gamma\eta'}(Q^2)|$ if the chiral limit given by Eqn. 6 held for η'. To estimate the value of $f_{\eta'}$ (74.4 MeV) we use Eqns. 4 and 6 and the tabulated two-photon partial width of η' of 4.3 keV [59].

We fit the $|\mathcal{F}_{\gamma^*\gamma\eta'}(Q^2)|^2$ distributions measured using each decay chain with the functional form given by Eqn. 8 and obtain the values of the pole-mass parameter $\Lambda_{\eta'}$ that are shown in Table XI. From a simultaneous fit to our six results for the production of η' we obtain the following value of the pole-mass parameter:

$$\Lambda_{\eta'} = 859 \pm 9 \pm 18 \pm 20 \text{ MeV}. \tag{15}$$

The result of this fit is shown in Fig. 23.

The results of our measurements for the production of η' demonstrate that if this particle were a $q\bar{q}$ bound state and the QCD chiral limit given by Eqn. 6 held for this meson, the Q^2-dependence of the transition form factor of η' and consequently its wave function would be significantly different from these non-perturbative properties of either π^0 or η.

VIII. CONCLUSIONS

We have measured the form factors associated with the electromagnetic transitions $\gamma^*\gamma \to$ meson in the regions of momentum transfer from 1.5 to 9, 20, and 30 GeV^2 for the π^0, η, and η' mesons, respectively. These are the first measurements above 2.7 GeV^2 for π^0 and above 7 GeV^2 for η and η'.

Our measurement for π^0 unambiguously distinguishes among various theoretical predictions for the form factors of the $\gamma^*\gamma \to \pi^0$ transition. We have demonstrated that the non-perturbative properties of π^0 and η agree with each other which indicates that the wave functions of these two mesons are similar. In the η' analysis we have shown that the non-perturbative properties of η' differ substantially from those of π^0 and η. Our measurement for η' provides important information for future theoretical investigations of the structure of this particle.

IX. ACKNOWLEDGEMENTS

We gratefully acknowledge the effort of the CESR staff in providing us with excellent luminosity and running conditions. J.P.A., J.R.P., and I.P.J.S. thank the NYI program of the NSF, M.S. thanks the PFF program of the NSF, G.E. thanks the Heisenberg Foundation, K.K.G., M.S., H.N.N., T.S., and H.Y. thank the OJI program of DOE, J.R.P., K.H., M.S. and V.S. thank the A.P. Sloan Foundation, A.W. and R.W. thank the Alexander von Humboldt Stiftung, and M.S. thanks Research Corporation for support. This work was supported by the National Science Foundation, the U.S. Department of Energy, and the Natural Sciences and Engineering Research Council of Canada.

[1] V. Savinov, PhD thesis, University of Minnesota, Minneapolis, 1997, Unpublished.

[2] V.M. Budnev *et al.*, *Phys. Rep.* **C15** (1975) 181.
[3] G.P. Lepage and S.J. Brodsky, *Phys. Rev.* **D22** (1980) 2157.
[4] S.J. Brodsky and G.P. Lepage, *Phys. Rev.* **D24** (1981) 1808.
[5] A.V. Efremov and A.V. Radyushkin, *Phys. Lett.* **B94** (1980) 245.
[6] V.L. Chernyak and A.R. Zhitnitsky, *Phys. Rep.* **112** (1984) 173.
[7] S. Adler, *Phys. Rev.* **177** (1969) 2426.
[8] J. Bell and R. Jackiw, *Nuovo. Cim.* **A60** (1969) 47.
[9] L.H. Ryder, Quantum Field Theory, p.297, Cambridge University Press, 1986.
[10] S. Coleman, Aspects of Symmetry, Cambridge University Press, 1985.
[11] M.A. Shifman, A.I. Vainshtein, V.I. Zakharov, *Nucl. Phys.* **B147** (1979) 385.
[12] P. Kroll, Universität Wuppertal preprint WU B 94-17. Also, hep-ph 9409262, 1994.
[13] R. Jakob *et al.*, *J. Phys.* **G22** (1996) 45.
[14] H.-N. Li and G. Sterman, *Nucl. Phys.* **B381** (1992) 129.
[15] V. Savinov, CLEO Coll., in the Proceedings of the Conference Photon'95, p.203, edited by David J. Miller *et al.*, World Scientific, 1995.
[16] F.-G. Cao *et al.*, *Phys. Rev.* **D53** (1996) 6582.
[17] H.-N. Li, *Phys. Rev.* **D48** (1993) 4243.
[18] J. Bolz *et al.*, *Phys. Lett.* **B342** (1995) 345.
[19] M. Dahm *et al.*, *Z. Phys.* **C68** (1995) 595.
[20] J. Bolz *et al.*, *Z. Phys.* **C66** (1995) 267.
[21] B. Chibisov and A.R. Zhitnitsky, *Phys. Rev.* **D52** (1995) 5273.
[22] N. Isgur and C.H. Llewellyn Smith, *Phys. Rev. Lett.* **52** (1984) 1080.
[23] J. Botts and G. Sterman, *Nucl. Phys.* **B325** (1984) 62.
[24] N. Isgur and C.H. Llewellyn Smith, *Nucl. Phys.* **B317** (1989) 526.
[25] R. Jakob and P. Kroll, *Phys. Lett.* **B315** (1993) 463.
[26] V. Braun and I. Halperin, *Phys. Lett.* **B328** (1994) 457.
[27] A.V. Radyushkin, in the Proceedings of the Workshop on CEBAF at Higher Energies, p.273, edited by N. Isgur and P. Stoler, CEBAF, 1994.
[28] A.R. Zhitnitsky, hep-ph 9605226, 1996.
[29] A.V. Efremov and A.V. Radyushkin, *Theor. Math. Phys.* **42** (1980) 97.
[30] A.V. Radyushkin, *Nucl. Phys.* **A532** (1991) 141.
[31] I.V. Musatov and A.V. Radyushkin, Thomas Jefferson National Accelerator Facility (formerly CEBAF) preprint JLAB-THY-97-07. Also, hep-ph 9702443, 1997.
[32] A.V. Radyushkin and R. Ruskov, *Phys. Lett.* **B374** (1996) 173.
[33] Private communication with A.V. Radyushkin and R. Ruskov.
[34] P. Ball, *Phys. Rev.* **D48** (1993) 3190.
[35] A. Khodjamirian and R. Rückl, Preprint WUE-ITP-96-020, also hep-ph 9610367, 1996.
[36] P. Ball and V.M. Braun, *Phys. Rev.* **D55** (1997) 5561.
[37] P. Kroll and M. Raulfs, *Phys. Lett.* **B387** (1996) 848.
[38] V.V. Anisovich *et al.*, *Phys. Rev.* **D55** (1997) 2918.
[39] A.E. Dorokhov, Universita di Pisa and INFN preprint IFUP - TH 36/95, July 1995.
[40] S. Ong, *Phys. Rev.* **D52** (1995) 3111.
[41] R.M. Davidson, to be published in the Proceedings of the Workshop on the Structure of the η' Meson, edited by N. Isgur and P. Stoler, New Mexico State University and CEBAF, Las Cruces, New Mexico, 1996.
[42] M.R. Frank *et al.*, *Phys. Lett.* **B359** (1995) 17.
[43] D. Kekez and D. Klabučar, *Phys. Lett.* **B387** (1996) 14.
[44] A. Anselm *et al.*, Harvard University preprint HUTP-95/A037. Also, hep-ph 9603444, 1996.
[45] V.M. Belyaev and M.B. Johnson, hep-ph 9605279, 1996.
[46] G. Sterman and P. Stoler, Hadronic Form Factors and Perturbative QCD. To be published in *Ann. Rev. of Nucl. and Part. Sc.*, 1997.
[47] R.I. Djhelyadin *et al.*, Lepton-G Exp., *Phys. Lett.* **B94** (1980) 548.
[48] Ch. Berger *et al.*, PLUTO Coll., *Phys. Lett.* **142** (1984) 125.
[49] H. Aihara *et al.*, TPC/2γ Coll., *Phys. Rev. Lett.* **64** (1990) 172.
[50] H.-J. Behrend *et al.*, CELLO Coll., *Z. Phys.* **C49** (1991) 401.
[51] Y. Kubota *et al.*, CLEO Coll., *Nucl. Inst. and Meth.* **A320** (1992) 66.
[52] C. Bebek *et al.*, CLEO Coll., *Nucl. Inst. and Meth.* **A302** (1992) 261.
[53] D.E. Acosta, PhD thesis, University of California, San Diego, 1993, Unpublished.
[54] B.H. Ong, PhD thesis, University of California, San Diego, 1993, Unpublished.
[55] TWOGAM. The Two-Photon Monte Carlo Simulation Program. Written by D.M. Coffman. Unpublished.

[56] J.J. Sakurai, *Ann. Phys.* **11** (1960) 1.
[57] A.V. Radyushkin and R. Ruskov, *Nucl. Phys.* **B481** (1996) 625.
[58] V.N. Gribov and I.Ya. Pomeranchuk, *Phys. Rev. Lett.* **8** (1962) 343.
[59] Particle Data Group, L. Montanet *et al.*, Review of Particle Properties, *Phys. Rev.* **D54** (1996) 1.
[60] "GEANT. Detector Description and Simulation Tool.", by Application Software Group, Computing and Networks Division. The CERN Program Library index W5013, CERN, Geneva, Switzerland.
[61] G. Crawford *et al.*, CLEO Coll., *Nucl. Inst. and Meth.* **A345** (1994) 429.
[62] W.L. van Neerven and J.A.M. Vermaseren, *Nucl. Phys.* **B238** (1984) 73.
[63] M. Landrø *et al.*, *Phys. Rev.* **D36** (1987) 44.
[64] M. Abramowitz and I.A. Stegun (eds.), Handbook of mathematical functions (National Bureau of Standards, Washington; D.C., 1964) The upper tail probability of the χ^2 distribution (P_{χ^2}) is the area of the χ^2 distribution with N degrees of freedom above measured χ^2 value. In our case the number of degrees of freedom is the number of available dE/dx measurements. The CERN Program Library index G100, CERN, Geneva, Switzerland.
[65] D. Müller, *Phys. Rev.* **D51** (1995) 3855.

TABLE I. The results of the $\pi^0 \to \gamma\gamma$ analysis assuming $\mathcal{B} \equiv \mathcal{B}(\pi^0 \to \gamma\gamma) = 0.99$. The differential cross section is for $e^+e^- \to e^+e^-\pi^0$.

Q^2 interval (GeV^2)	N_{π^0} detected	N_{π^0} signal	ϵ %	$\mathcal{B} \times N_{\pi^0}$ produced	$\tilde{Q}^2$ (GeV^2)	$d\sigma/dQ^2(\tilde{Q}^2)$ (fb / GeV^2)	$\tilde{Q}^2\lvert\mathcal{F}_{\gamma^*\gamma\pi^0}(\tilde{Q}^2)\rvert$ (0.01 × GeV)
1.5 – 1.8	150 ± 16	137 ± 17	7.5	1831 ± 231	1.64	2145 ± 270 ± 105	12.1 ± 0.8 ± 0.3
1.8 – 2.0	174 ± 19	163 ± 20	24	686 ± 82	1.90	1205 ± 144 ± 59	11.7 ± 0.7 ± 0.3
2.0 – 2.2	193 ± 19	182 ± 20	26	688 ± 74	2.10	1209 ± 131 ± 59	13.8 ± 0.8 ± 0.3
2.2 – 2.4	125 ± 16	120 ± 16	28	424 ± 57	2.30	744 ± 100 ± 37	12.7 ± 0.9 ± 0.3
2.4 – 2.6	106 ± 15	101 ± 15	29	355 ± 52	2.50	624 ± 92 ± 31	13.5 ± 1.0 ± 0.3
2.6 – 2.8	102 ± 14	99 ± 15	29	342 ± 50	2.70	602 ± 89 ± 30	15.1 ± 1.1 ± 0.4
2.8 – 3.1	99 ± 15	88 ± 16	29	309 ± 56	2.94	362 ± 65 ± 18	13.7 ± 1.2 ± 0.3
3.1 – 3.5	107 ± 15	97 ± 16	30	321 ± 53	3.29	282 ± 47 ± 14	14.5 ± 1.2 ± 0.4
3.5 – 4.0	75 ± 13	65 ± 14	31	213 ± 46	3.74	150 ± 32 ± 7	13.2 ± 1.4 ± 0.3
4.0 – 4.5	43 ± 10	43 ± 10	31	138 ± 31	4.24	97 ± 22 ± 5	13.4 ± 1.5 ± 0.3
4.5 – 5.0	40 ± 9	40 ± 9	33	122 ± 26	4.74	85 ± 18 ± 4	15.4 ± 1.7 ± 0.4
5.0 – 5.5	26 ± 6	26 ± 6	34	76 ± 18	5.24	54 ± 13 ± 3	14.5 ± 1.8 ± 0.4
5.5 – 6.0	20 ± 6	20 ± 6	32	63 ± 18	5.74	44 ± 12 ± 2	15.5 ± 2.2 ± 0.4
6.0 – 7.0	23 ± 6	23 ± 6	31	74 ± 20	6.47	26 ± 7 ± 1	14.8 ± 2.0 ± 0.4
7.0 – 9.0	15 ± 5	15 ± 5	16	94 ± 28	7.90	17 ± 5 ± 1	16.7 ± 2.5 ± 0.4

TABLE II. The results of the $\eta \to \gamma\gamma$ analysis assuming $\mathcal{B} \equiv \mathcal{B}(\eta \to \gamma\gamma) = 0.39$. The differential cross section is for $e^+e^- \to e^+e^-\eta$.

Q^2 interval (GeV^2)	N_η detected	N_η signal	ϵ %	$\mathcal{B} \times N_\eta$ produced	$\tilde{Q}^2$ (GeV^2)	$d\sigma/dQ^2(\tilde{Q}^2)$ (fb / GeV^2)	$\tilde{Q}^2\lvert\mathcal{F}_{\gamma^*\gamma\eta}(\tilde{Q}^2)\rvert$ (0.01 × GeV)
1.5 – 2.0	73 ± 12	73 ± 12	9.4	768 ± 131	1.73	1359 ± 231 ± 67	10.9 ± 0.9 ± 0.3
2.0 – 2.5	81 ± 14	81 ± 14	21	392 ± 66	2.23	694 ± 117 ± 34	12.0 ± 1.0 ± 0.3
2.5 – 3.0	59 ± 10	59 ± 10	22	264 ± 47	2.74	467 ± 83 ± 23	13.9 ± 1.2 ± 0.3
3.0 – 3.5	35 ± 8	35 ± 8	25	142 ± 33	3.24	251 ± 59 ± 12	13.6 ± 1.6 ± 0.3
3.5 – 4.0	19 ± 7	19 ± 7	24	78 ± 29	3.74	138 ± 51 ± 7	12.8 ± 2.4 ± 0.3
4.0 – 5.0	28 ± 8	28 ± 8	27	105 ± 29	4.46	93 ± 26 ± 5	14.5 ± 2.0 ± 0.4
5.0 – 6.5	22 ± 6	22 ± 6	28	79 ± 22	5.68	47 ± 13 ± 2	15.7 ± 2.2 ± 0.4
6.5 – 9.0	8 ± 3	8 ± 3	18	46 ± 19	7.58	16 ± 7 ± 1	15.3 ± 3.2 ± 0.4

TABLE III. The results of the $\eta \to 3\pi^0$ analysis assuming $\mathcal{B} \equiv \mathcal{B}(\eta \to 3\pi^0)\times\, \mathcal{B}^3(\pi^0 \to \gamma\gamma) = 0.31$. The differential cross section is for $e^+e^- \to e^+e^-\eta$.

Q^2 interval (GeV^2)	N_η detected	N_η signal	ϵ %	$\mathcal{B} \times N_\eta$ produced	$\tilde{Q}^2$ (GeV^2)	$d\sigma/dQ^2(\tilde{Q}^2)$ (fb / GeV^2)	$\tilde{Q}^2\lvert\mathcal{F}_{\gamma^*\gamma\eta}(\tilde{Q}^2)\rvert$ (0.01 × GeV)
1.5 – 2.0	39 ± 7	37 ± 7	6.9	544 ± 95	1.73	1219 ± 212 ± 90	10.3 ± 0.9 ± 0.4
2.0 – 2.5	57 ± 8	54 ± 8	14	392 ± 57	2.23	879 ± 128 ± 65	13.5 ± 1.0 ± 0.5
2.5 – 3.5	47 ± 7	45 ± 7	16	279 ± 44	2.94	312 ± 50 ± 23	12.9 ± 1.0 ± 0.4
3.5 – 5.6	24 ± 5	24 ± 5	18	132 ± 31	4.16	99 ± 23 ± 7	13.1 ± 1.5 ± 0.4
5.6 – 9.0	20 ± 5	20 ± 5	15	135 ± 34	6.56	38 ± 10 ± 3	18.3 ± 2.3 ± 0.7

TABLE IV. The results of the $\eta \to \pi^+\pi^-\pi^0$ analysis assuming $\mathcal{B} \equiv \mathcal{B}(\eta \to \pi^+\pi^-\pi^0)\times\ \mathcal{B}(\pi^0 \to \gamma\gamma) = 0.23$. The differential cross section is for $e^+e^- \to e^+e^-\eta$.

Q^2 interval (GeV^2)	N_η detected	N_η signal	ϵ %	$\mathcal{B}\times N_\eta$ produced	$\tilde{Q}^2$ (GeV^2)	$d\sigma/dQ^2(\tilde{Q}^2)$ (fb / GeV^2)	$\tilde{Q}^2\lvert\mathcal{F}_{\gamma^*\gamma\eta}(\tilde{Q}^2)\rvert$ (0.01 × GeV)
1.5 – 2.0	37 ± 6	37 ± 6	10	385 ± 67	1.73	1167 ± 202 ± 90	10.1 ± 0.87 ± 0.39
2.0 – 2.5	51 ± 7	50 ± 7	21	235 ± 35	2.23	714 ± 105 ± 55	12.1 ± 0.89 ± 0.47
2.5 – 3.5	49 ± 7	48 ± 7	23	210 ± 31	2.94	318 ± 47 ± 25	13.0 ± 0.96 ± 0.50
3.5 – 5.0	31 ± 6	31 ± 6	26	117 ± 23	4.16	118 ± 23 ± 9	14.4 ± 1.39 ± 0.55
5.0 – 9.0	32 ± 6	32 ± 6	26	122 ± 23	6.56	46 ± 9 ± 4	20.1 ± 1.88 ± 0.77
9.0 – 20.0	6 ± 3	6 ± 3	25	23 ± 10	12.74	3.1 ± 1.4 ± 0.2	18.4 ± 4.19 ± 0.71

TABLE V. The results of the $\eta' \to \pi^0\pi^0\eta \to 6\gamma$ analysis assuming $\mathcal{B} \equiv \mathcal{B}(\eta' \to \pi^0\pi^0\eta) \times \mathcal{B}(\eta \to \gamma\gamma)\times$ $\mathcal{B}^2(\pi^0 \to \gamma\gamma) = 0.080$. The differential cross section is for $e^+e^- \to e^+e^-\eta'$.

Q^2 interval (GeV^2)	$N_{\eta'}$ detected	$N_{\eta'}$ signal	ϵ %	$\mathcal{B}\times N_{\eta'}$ produced	$\tilde{Q}^2$ (GeV^2)	$d\sigma/dQ^2(\tilde{Q}^2)$ (fb / GeV^2)	$\tilde{Q}^2\lvert\mathcal{F}_{\gamma^*\gamma\eta'}(\tilde{Q}^2)\rvert$ (0.01 × GeV)
1.5 – 2.0	40 ± 7	40 ± 7	8.4	474 ± 85	1.73	4132 ± 740 ± 310	20.1 ± 1.8 ± 0.8
2.0 – 2.5	40 ± 7	40 ± 7	16	259 ± 44	2.23	2258 ± 381 ± 169	22.7 ± 1.9 ± 0.9
2.5 – 3.5	29 ± 6	29 ± 6	16	176 ± 38	2.94	767 ± 164 ± 58	21.1 ± 2.3 ± 0.8
3.5 – 5.0	17 ± 4	17 ± 4	18	94 ± 24	4.16	274 ± 70 ± 21	22.7 ± 2.9 ± 0.9
5.0 – 9.0	14 ± 4	14 ± 4	16	90 ± 24	6.56	98 ± 26 ± 7	30.0 ± 4.0 ± 1.1

TABLE VI. The results of the $\eta' \to \pi^0\pi^0\eta \to 5\pi^0 \to 10\gamma$ analysis assuming $\mathcal{B} \equiv \mathcal{B}(\eta' \to \pi^0\pi^0\eta)\times\ \mathcal{B}(\eta \to 3\pi^0)\times$ $\mathcal{B}^5(\pi^0 \to \gamma\gamma) = 0.063$. The differential cross section is for $e^+e^- \to e^+e^-\eta'$.

Q^2 interval (GeV^2)	$N_{\eta'}$ detected	$N_{\eta'}$ signal	ϵ %	$\mathcal{B}\times N_{\eta'}$ produced	$\tilde{Q}^2$ (GeV^2)	$d\sigma/dQ^2(\tilde{Q}^2)$ (fb / GeV^2)	$\tilde{Q}^2\lvert\mathcal{F}_{\gamma^*\gamma\eta'}(\tilde{Q}^2)\rvert$ (0.01 × GeV)
1.5 – 3.0	18 ± 5	18 ± 5	3.5	510 ± 153	2.09	1875 ± 563 ± 204	18.6 ± 2.8 ± 1.0
3.0 – 9.0	7 ± 3	7 ± 2	5.4	129 ± 49	4.92	118 ± 45 ± 13	20.0 ± 3.8 ± 1.1

TABLE VII. The results of the $\eta' \to \rho^0\gamma \to \pi^+\pi^-\gamma$ analysis assuming $\mathcal{B} \equiv \mathcal{B}(\eta' \to \rho^0\gamma)\times\ \mathcal{B}(\rho^0 \to \pi^+\pi^-) = 0.30$. The differential cross section is for $e^+e^- \to e^+e^-\eta'$.

Q^2 interval (GeV^2)	$N_{\eta'}$ detected	$N_{\eta'}$ signal	ϵ %	$\mathcal{B}\times N_{\eta'}$ produced	$\tilde{Q}^2$ (GeV^2)	$d\sigma/dQ^2(\tilde{Q}^2)$ (fb / GeV^2)	$\tilde{Q}^2\lvert\mathcal{F}_{\gamma^*\gamma\eta'}(\tilde{Q}^2)\rvert$ (0.01 × GeV)
1.5 – 2.0	111 ± 13	111 ± 13	8.9	1257 ± 152	1.73	2891 ± 350 ± 197	16.8 ± 1.02 ± 0.57
2.0 – 2.5	131 ± 14	131 ± 14	17	765 ± 84	2.23	1759 ± 193 ± 120	20.0 ± 1.10 ± 0.68
2.5 – 3.5	123 ± 14	123 ± 14	21	593 ± 69	2.94	681 ± 79 ± 46	19.9 ± 1.15 ± 0.68
3.5 – 5.0	86 ± 11	86 ± 11	24	353 ± 47	4.16	270 ± 36 ± 18	22.6 ± 1.51 ± 0.77
5.0 – 9.0	49 ± 10	49 ± 10	31	158 ± 32	6.56	45 ± 9 ± 3	20.4 ± 2.08 ± 0.69
9.0 – 30.0	22 ± 8	22 ± 8	37	58 ± 21	15.30	3.2 ± 1.1 ± 0.2	24.8 ± 4.44 ± 0.84

TABLE VIII. The results of the $\eta' \rightarrow \pi^+\pi^-\eta \rightarrow \pi^+\pi^-2\gamma$ analysis assuming $\mathcal{B} \equiv \mathcal{B}(\eta' \rightarrow \eta\pi^+\pi^-)\times \mathcal{B}(\eta \rightarrow \gamma\gamma) = 0.17$. The differential cross section is for $e^+e^- \rightarrow e^+e^-\eta'$.

Q^2 interval (GeV^2)	$N_{\eta'}$ detected	$N_{\eta'}$ signal	ϵ %	$\mathcal{B} \times N_{\eta'}$ produced	$\tilde{Q}^2$ (GeV^2)	$d\sigma/dQ^2(\tilde{Q}^2)$ (fb / GeV^2)	$\tilde{Q}^2\lvert\mathcal{F}_{\gamma^*\gamma\eta'}(\tilde{Q}^2)\rvert$ ($0.01 \times$ GeV)
1.5 – 2.0	57 ± 8	57 ± 8	7.6	743 ± 104	1.73	3007 ± 421 ± 199	17.1 ± 1.2 ± 0.6
2.0 – 2.5	70 ± 9	70 ± 9	17	408 ± 51	2.23	1651 ± 208 ± 109	19.4 ± 1.2 ± 0.6
2.5 – 3.5	60 ± 8	60 ± 8	21	282 ± 38	2.94	570 ± 77 ± 38	18.2 ± 1.2 ± 0.6
3.5 – 5.0	58 ± 8	58 ± 8	27	216 ± 30	4.16	292 ± 40 ± 19	23.5 ± 1.6 ± 0.8
5.0 – 9.0	45 ± 7	45 ± 7	34	133 ± 20	6.56	67 ± 10 ± 4	24.9 ± 1.9 ± 0.8
9.0 – 30.0	16 ± 4	16 ± 4	36	44 ± 11	15.30	4.3 ± 1.1 ± 0.3	28.8 ± 3.6 ± 0.9

TABLE IX. The results of the $\eta' \rightarrow \pi^+\pi^-\eta \rightarrow 2\pi^+2\pi^-\pi^0 \rightarrow 2\pi^+2\pi^-2\gamma$ analysis assuming $\mathcal{B} \equiv \mathcal{B}(\eta' \rightarrow \pi^+\pi^-\eta)\times \mathcal{B}(\eta \rightarrow \pi^+\pi^-\pi^0)\times \mathcal{B}(\pi^0 \rightarrow \gamma\gamma) = 0.10$. The differential cross section is for $e^+e^- \rightarrow e^+e^-\eta'$.

Q^2 interval (GeV^2)	$N_{\eta'}$ detected	$N_{\eta'}$ signal	ϵ %	$\mathcal{B} \times N_{\eta'}$ produced	$\tilde{Q}^2$ (GeV^2)	$d\sigma/dQ^2(\tilde{Q}^2)$ (fb / GeV^2)	$\tilde{Q}^2\lvert\mathcal{F}_{\gamma^*\gamma\eta'}(\tilde{Q}^2)\rvert$ ($0.01 \times$ GeV)
1.5 – 2.5	33 ± 6	33 ± 6	6.2	528 ± 95	1.92	1830 ± 329 ± 176	15.9 ± 1.4 ± 0.7
2.5 – 3.5	22 ± 5	22 ± 5	13	169 ± 40	2.94	584 ± 138 ± 56	18.4 ± 2.2 ± 0.9
3.5 – 5.0	18 ± 5	18 ± 5	16	113 ± 30	4.16	261 ± 69 ± 25	22.2 ± 2.9 ± 1.1
5.0 – 9.0	15 ± 4	15 ± 4	21	74 ± 20	6.56	64 ± 17 ± 6	24.4 ± 3.2 ± 1.2
9.0 – 30.0	4 ± 2	4 ± 2	24	16 ± 8	15.30	2.7 ± 1.4 ± 0.3	22.9 ± 5.8 ± 1.1

TABLE X. The results of the $\eta' \rightarrow \pi^+\pi^-3\pi^0 \rightarrow \pi^+\pi^-6\gamma$ analysis assuming $\mathcal{B} \equiv (\mathcal{B}(\eta' \rightarrow \pi^+\pi^-\eta)\times \mathcal{B}(\eta \rightarrow 3\pi^0)+ \mathcal{B}(\eta' \rightarrow \pi^0\pi^0\eta)\times \mathcal{B}(\eta \rightarrow \pi^+\pi^-\pi^0)) \times \mathcal{B}^3(\pi^0 \rightarrow \gamma\gamma) = 0.14$. The differential cross section is for $e^+e^- \rightarrow e^+e^-\eta'$.

Q^2 interval (GeV^2)	$N_{\eta'}$ detected	$N_{\eta'}$ signal	ϵ %	$\mathcal{B} \times N_{\eta'}$ produced	$\tilde{Q}^2$ (GeV^2)	$d\sigma/dQ^2(\tilde{Q}^2)$ (fb / GeV^2)	$\tilde{Q}^2\lvert\mathcal{F}_{\gamma^*\gamma\eta'}(\tilde{Q}^2)\rvert$ ($0.01 \times$ GeV)
1.5 – 2.5	54 ± 8	54 ± 8	3.7	1468 ± 206	1.92	2803 ± 393 ± 247	19.7 ± 1.4 ± 0.9
2.5 – 3.5	25 ± 6	25 ± 6	7.5	330 ± 78	2.94	630 ± 149 ± 55	19.1 ± 2.3 ± 0.8
3.5 – 5.0	15 ± 4	15 ± 4	10	161 ± 45	4.16	205 ± 57 ± 18	19.7 ± 2.7 ± 0.9
5.0 – 9.0	13 ± 4	13 ± 4	13	101 ± 34	6.56	48 ± 16 ± 4	21.0 ± 3.5 ± 0.9
9.0 – 30.0	2 ± 1	2 ± 1	15	14 ± 10	15.30	1.3 ± 0.9 ± 0.1	15.7 ± 5.6 ± 0.7

TABLE XI. Values of the pole-mass parameters Λ_{π^0}, Λ_η and $\Lambda_{\eta'}$ measured using various final states. For each measurement, the first error is statistical, the second error represents the systematic uncertainties of our measurement and the third error reflects the experimental error in the value of the two-photon partial width of the meson.

Decay chain	$\Lambda_{\mathcal{R}}$ (MeV)
$\pi^0 \to \gamma\gamma$	776 ± 10 ± 12 ± 16
$\eta \to \gamma\gamma$	778 ± 19 ± 12 ± 22
$\eta \to 3\pi^0 \to 6\gamma$	773 ± 20 ± 17 ± 22
$\eta \to \pi^+\pi^-\pi^0 \to \pi^+\pi^-2\gamma$	773 ± 18 ± 18 ± 22
Simultaneous fit to all η data	774 ± 11 ± 16 ± 22
$\eta' \to \rho^0\gamma \to \pi^+\pi^-\gamma$	857 ± 15 ± 19 ± 19
$\eta' \to \pi^+\pi^-\eta \to \pi^+\pi^-2\gamma$	864 ± 16 ± 18 ± 19
$\eta' \to \pi^+\pi^-3\pi^0 \to \pi^+\pi^-6\gamma$	838 ± 27 ± 21 ± 17
$\eta' \to \pi^+\pi^-\eta \to 2\pi^+2\pi^-2\gamma$	824 ± 29 ± 25 ± 18
$\eta' \to \pi^0\pi^0\eta \to 6\gamma$	931 ± 29 ± 21 ± 23
$\eta' \to \pi^0\pi^0\eta \to 10\gamma$	837 ± 61 ± 27 ± 17
Simultaneous fit to all η' data	859 ± 9 ± 18 ± 20

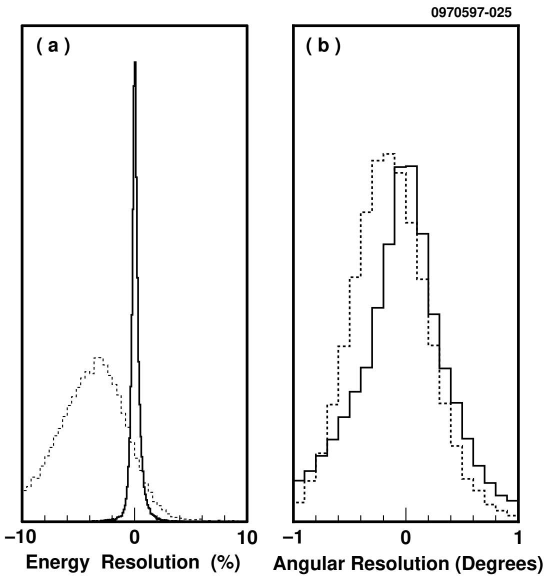

FIG. 1. Resolution functions of a) energy (in %) and b) scattering angle (in degrees) obtained from MC simulation in the π^0 analysis. Dashed and solid lines show resolution functions measured directly in the calorimeter and achieved using energy-momentum conservation, respectively.

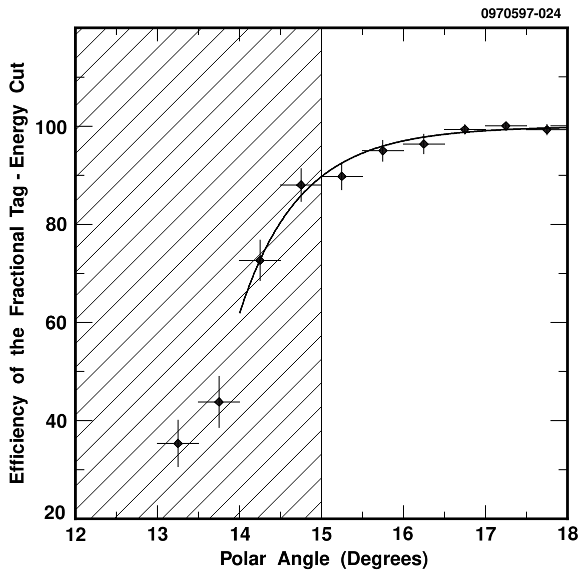

FIG. 2. The efficiency (in %) of the fractional tag-energy cut as measured from data. The solid line shows a power law approximation chosen to interpolate between the efficiency measurements. Events with tags scattered at polar angles less than 15° are rejected from all analyses.

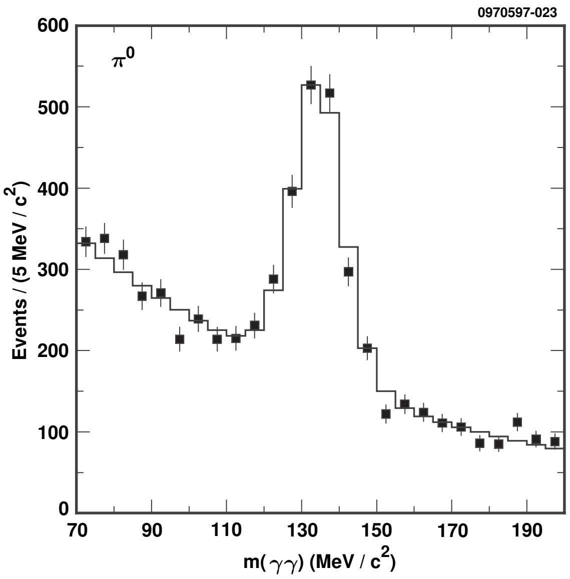

FIG. 3. Fit (solid line) to the $\gamma\gamma$ invariant mass distribution observed in data (points with error bars) in the $\pi^0 \to \gamma\gamma$ analysis. The signal line shape is obtained from the MC simulation, the remaining random background is approximated by an exponential.

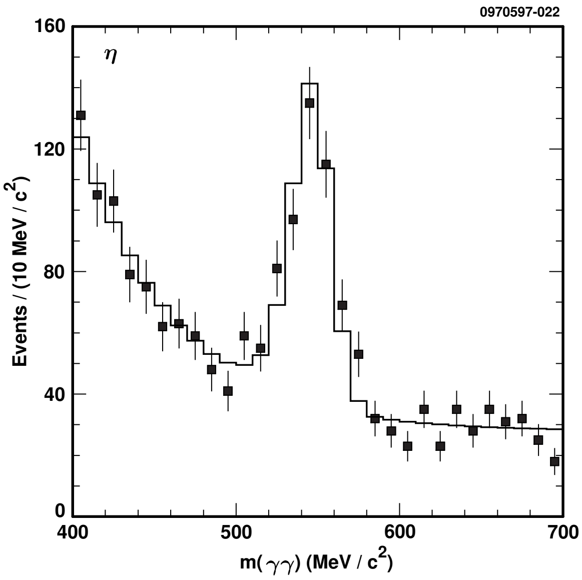

FIG. 4. Fit (solid line) to the $\gamma\gamma$ invariant mass distribution observed in data (points with error bars) in the $\eta \to \gamma\gamma$ analysis. The signal line shape is obtained from the MC simulation, the remaining random background is approximated by the sum of an exponential and a constant.

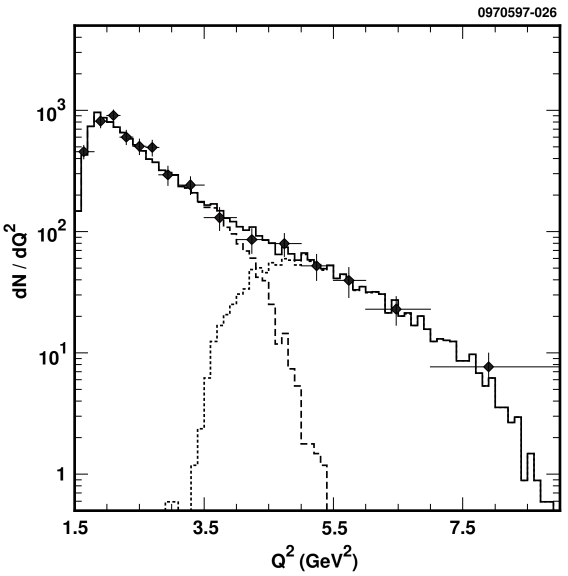

FIG. 5. The Q^2 distributions for signal π^0 events in MC (solid line) and data (points with error bars) in the $\pi^0 \to \gamma\gamma$ analysis. The distributions for events which belong to the energy- and track-tagged MC samples are shown with dashed and dotted lines, respectively. For each Q^2 interval in data the number of signal events is obtained from the fit followed by the background subtraction. The number of MC events is normalized to the number of signal π^0 events in data.

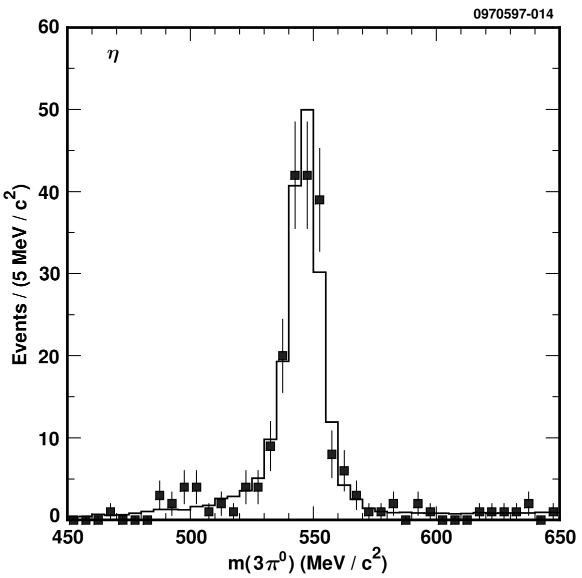

FIG. 6. Fit (solid line) to the $3\pi^0$ invariant mass distribution observed in data (points with error bars) in the $\eta \to 6\gamma$ analysis. The signal line shape is obtained from the MC simulation, the remaining random background is approximated by a first-order polynomial.

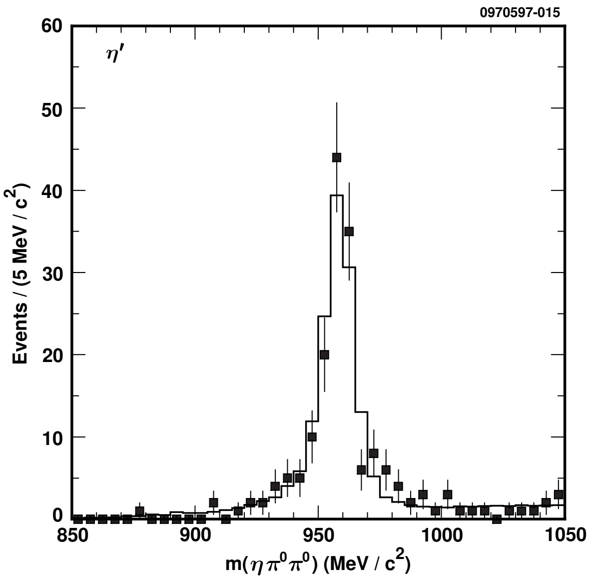

FIG. 7. Fit (solid line) to the $\pi^0\pi^0\eta \to 6\gamma$ invariant mass distribution observed in data (points with error bars) in the $\eta' \to 6\gamma$ analysis. The signal line shape is obtained from the MC simulation, the remaining random background is approximated by a first-order polynomial.

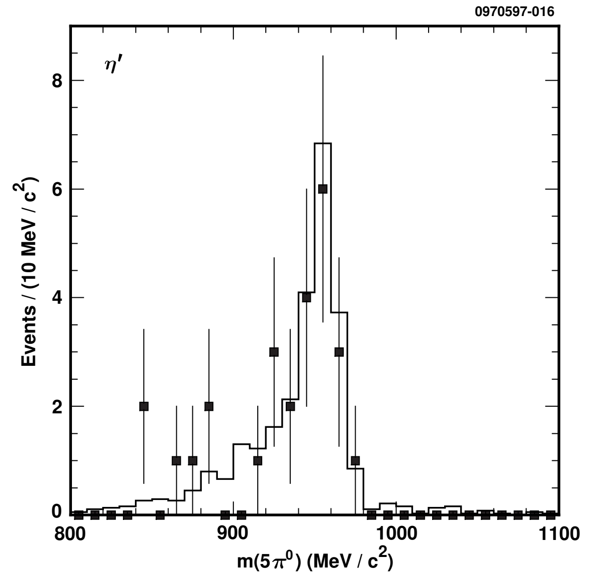

FIG. 8. Fit (solid line) to the $5\pi^0$ invariant mass distribution observed in data (points with error bars) in the $\eta' \to 10\gamma$ analysis. The signal line shape is obtained from the MC simulation, the remaining random background is approximated by a first-order polynomial.

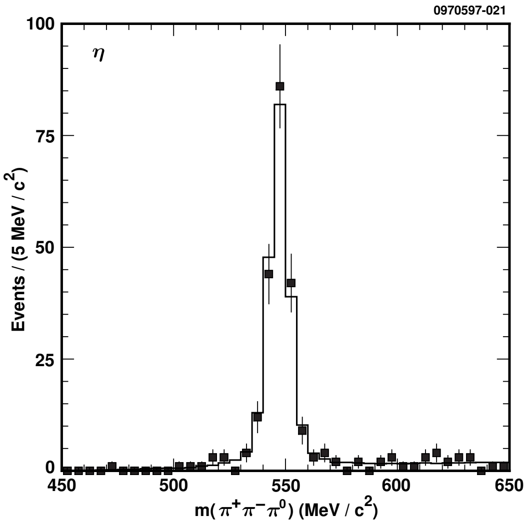

FIG. 9. Fit (solid line) to the $\pi^+\pi^-\pi^0$ invariant mass distribution observed in data (points with error bars) in the $\eta \to \pi^+\pi^-2\gamma$ analysis. The signal line shape is obtained from the MC simulation, the remaining random background is approximated by a first-order polynomial.

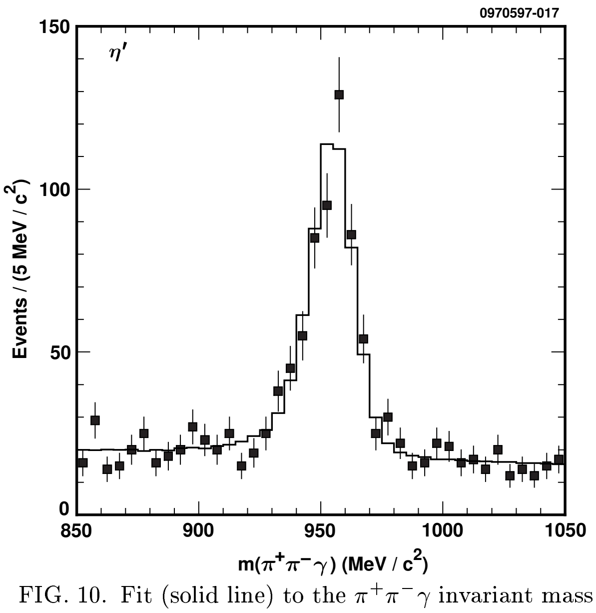

FIG. 10. Fit (solid line) to the $\pi^+\pi^-\gamma$ invariant mass distribution observed in data (points with error bars) in the $\eta' \to \pi^+\pi^-\gamma$ analysis. The signal line shape is obtained from the MC simulation, the remaining random background is approximated by a first-order polynomial.

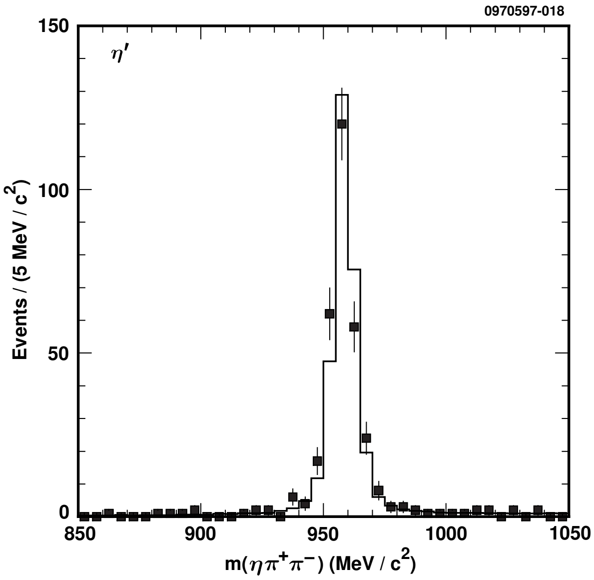

FIG. 11. Fit (solid line) to the $\pi^+\pi^-\eta \to \pi^+\pi^-2\gamma$ invariant mass distribution observed in data (points with error bars) in the $\eta' \to \pi^+\pi^-2\gamma$ analysis. The signal line shape is obtained from the MC simulation, the remaining random background is approximated by a first-order polynomial.

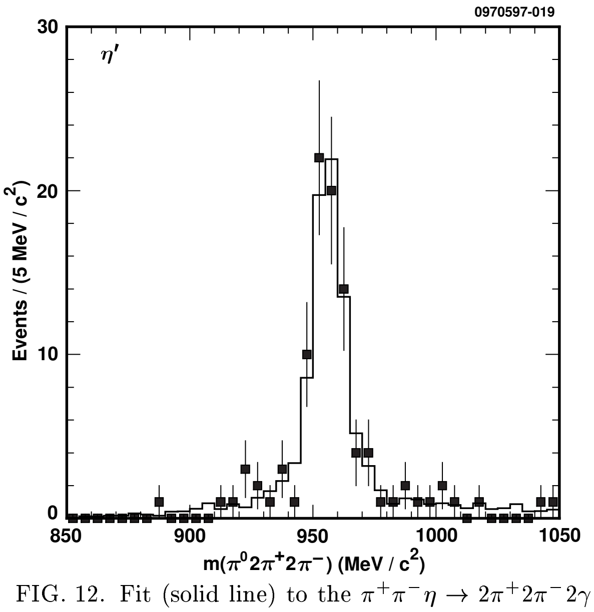

FIG. 12. Fit (solid line) to the $\pi^+\pi^-\eta \to 2\pi^+2\pi^-2\gamma$ invariant mass distribution observed in data (points with error bars) in the $\eta' \to 2\pi^+2\pi^-2\gamma$ analysis. The signal line shape is obtained from the MC simulation, the remaining random background is approximated by a first-order polynomial.

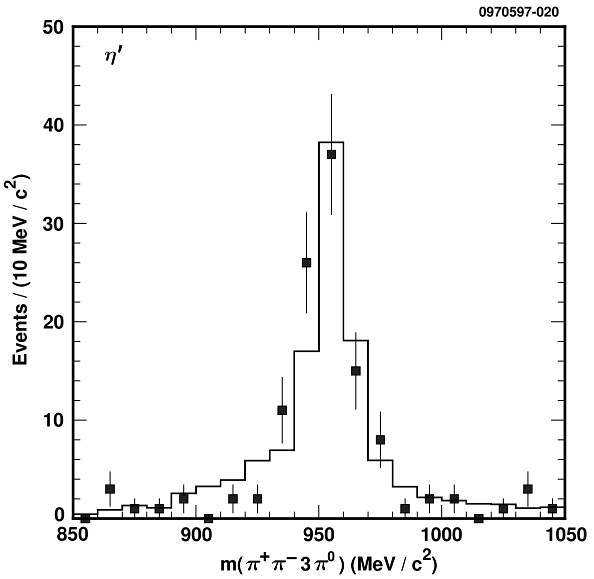

FIG. 13. Fit (solid line) to the $\pi^+\pi^-3\pi^0$ invariant mass distribution observed in data (points with error bars) in the $\eta' \to \pi^+\pi^-6\gamma$ analysis. The signal line shape is obtained from the MC simulation, the remaining random background is approximated by a first-order polynomial.

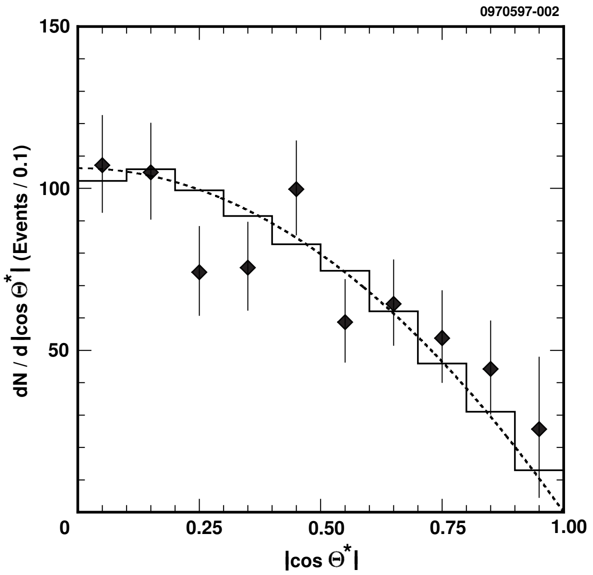

FIG. 15. Distribution of $|\cos\theta^*|$ in the $\eta' \to \rho^0\gamma$ analysis in data (points with error bars) and the MC simulation (histogram). The dotted line shows the $\sin^2\theta^*$ curve. The prediction of the MC simulation and $\sin^2\theta^*$ curve are normalized to the number of data events.

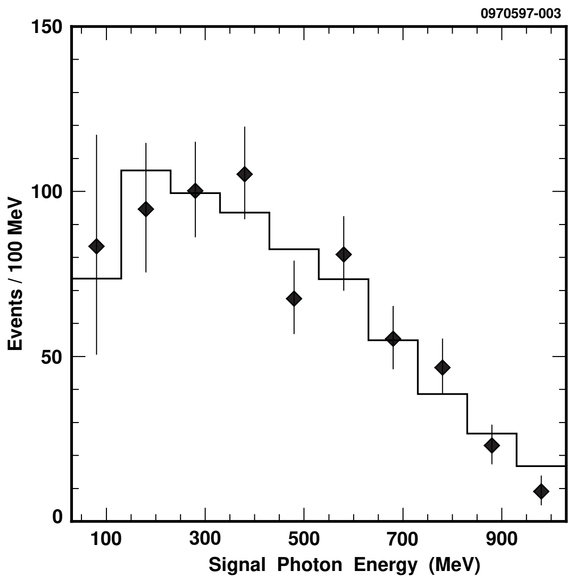

FIG. 14. Distribution of signal photon energy in the $\eta' \to \rho^0\gamma$ analysis in data (points with error bars) and the MC simulation (histogram). The prediction of the MC simulation is normalized to the number of data events.

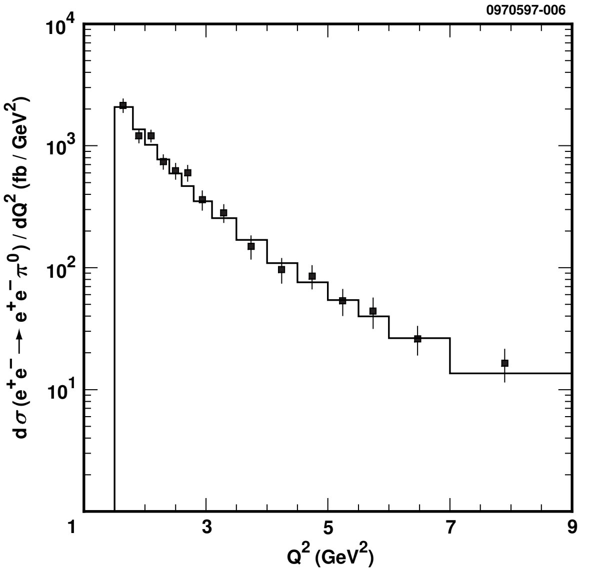

FIG. 16. Measured (points with error bars) and numerically estimated (histogram) differential cross sections for π^0 production.

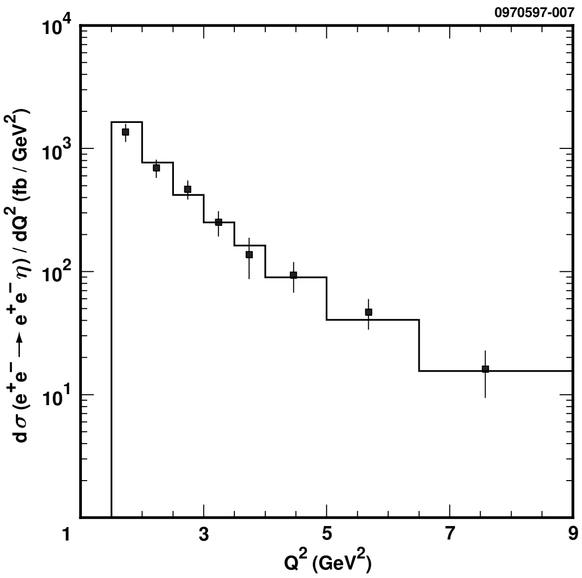

FIG. 17. Measured (points with error bars) and numerically estimated (histogram) differential cross sections for η production in the $\eta \to \gamma\gamma$ analysis.

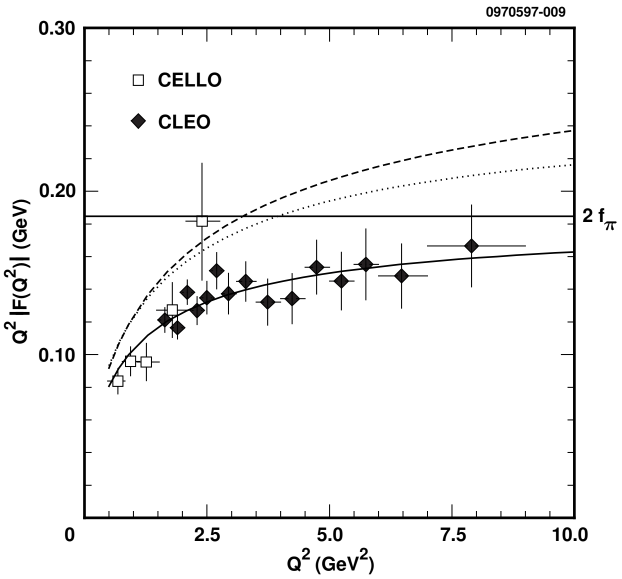

FIG. 18. Comparison of the results (points) for $Q^2|\mathcal{F}_{\gamma^*\gamma\pi^0}(Q^2)|$ with the theoretical predictions made by Jakob *et al.* [13] with the asymptotic wave function (solid curve) and the CZ wave function (dashed curve). The dotted curve shows the prediction made with the CZ wave function when its QCD evolution is taken into account.

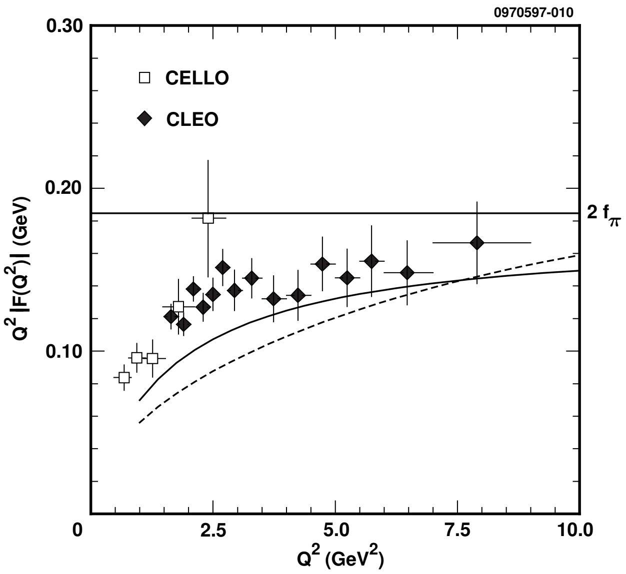

FIG. 19. Comparison of the results (points) for $Q^2|\mathcal{F}_{\gamma^*\gamma\pi^0}(Q^2)|$ with the theoretical predictions made by Cao *et al.* [16] with the asymptotic wave function (solid curve) and the CZ wave function (dashed curve).

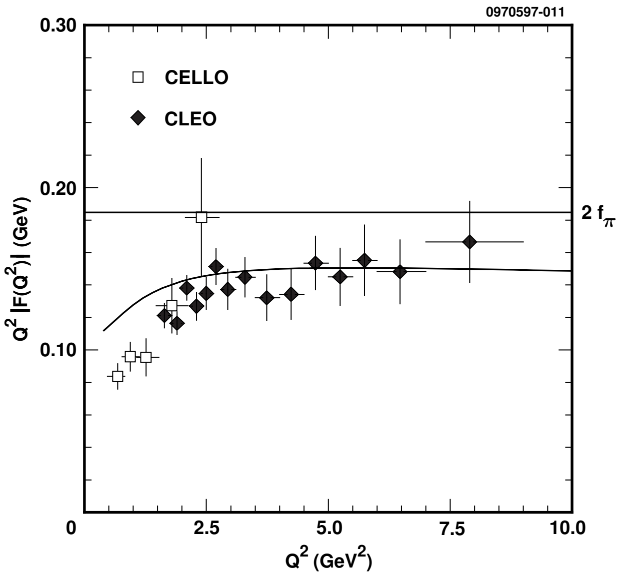

FIG. 20. Comparison of the results (points) for $Q^2|\mathcal{F}_{\gamma^*\gamma\pi^0}(Q^2)|$ with the theoretical prediction (curve) made by Radyushkin *et al.* [57].

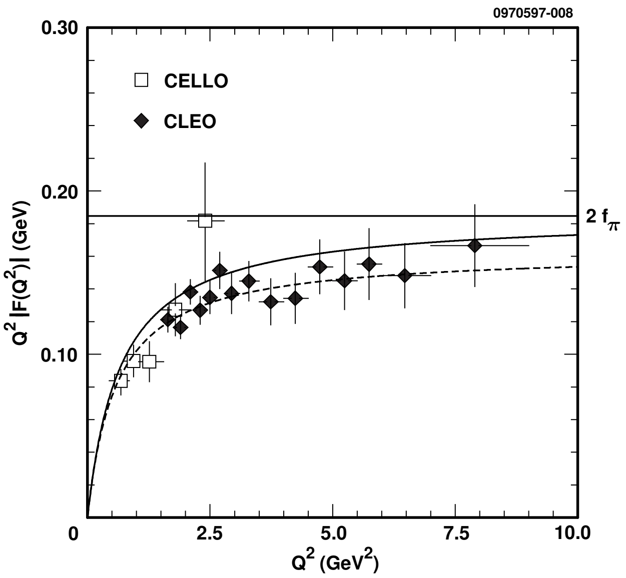

FIG. 21. The interpolation given by Eqn. 7 (solid curve) and the pole-mass parameter fit (dashed curve) to our results (closed circles) for $|\mathcal{F}_{\gamma^*\gamma\pi^0}(Q^2)|^2$ represented in the $Q^2|\mathcal{F}_{\gamma^*\gamma\pi^0}(Q^2)|$ form.

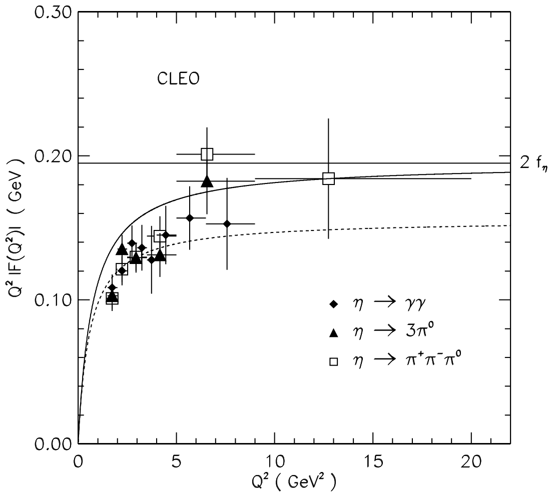

FIG. 22. Results of the pole-mass parameter fit to our results (points) for $|\mathcal{F}_{\gamma^*\gamma\eta}(Q^2)|^2$ represented in the $Q^2|\mathcal{F}_{\gamma^*\gamma\eta}(Q^2)|$ form (dashed line). The solid curve shows the interpolation given by Eqn. 7.

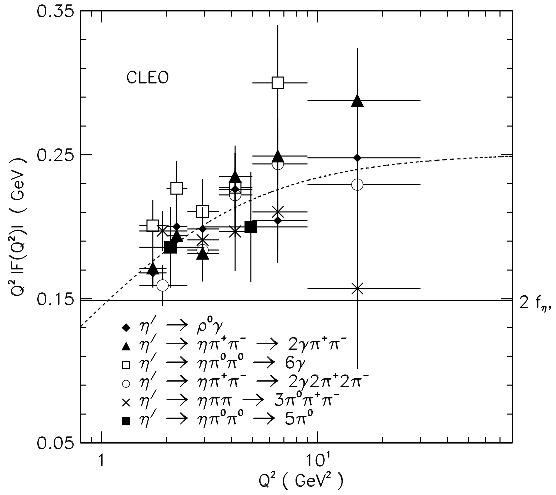

FIG. 23. Results of the pole-mass parameter fit to our results (points) for $|\mathcal{F}_{\gamma^*\gamma\eta'}(Q^2)|^2$ represented in the $Q^2|\mathcal{F}_{\gamma^*\gamma\eta'}(Q^2)|$ form (dashed line).